

# Subseasonal-to-interannual variability of rainfall over New Caledonia (SW Pacific)

Vincent Moron<sup>1,2,3</sup> · Renaud Barbero<sup>4</sup> · Andrew W. Robertson<sup>2,3</sup>

Received: 9 February 2015 / Accepted: 9 June 2015  
© Springer-Verlag Berlin Heidelberg 2015

**Abstract** Daily rainfall occurrence and amount at 55 stations over New Caledonia (NC, 20°S, 166°E) are examined throughout the calendar year during 1980–2010 using a Hidden Markov Model (HMM). Daily rainfall variability is described in terms of six discrete rainfall states identified by the HMM. Three states are interpreted as trade wind regimes associated with persistent low level anticyclonic conditions and weak to strong easterlies. The most prevalent state (state 1; 36 % of days) is dry everywhere and is characterized by an elongated anticyclone centered around Australia; NC is located on the eastern edge of this anticyclone. This state is predominant from mid-May to mid-December and peaks in September. The second most prevalent state (state 2; 27 % of days) and the last trade regime (state 4; 12 % of days) are most frequent in austral summer. States 2 and 4 are associated with the subtropical anticyclone centered south of NC, close to

its climatological location in austral summer, and light (state 2) to moderate (state 4) rainfall mostly along the windward coast. A distinct state (state 3; 11 % of days) is mostly associated with wintertime extratropical eastward traveling troughs between New Caledonia and New Zealand, inducing light rainfall over the SW of the main island of New Caledonia. The two last states 5 and 6 are infrequent (<15 % of days) but account for almost 70 % of total rainfall across the archipelago. They occur mostly in austral summer with their frequency of occurrence peaking in late February–early March. These states are associated with synoptic wave traveling eastward from eastern Australia leading to a strong influx of moisture from the equatorial latitudes when the associated cyclonic centre is located west of New Caledonia. The wettest state is also strongly modulated by intra-seasonal 15–80 days variability. These events contribute to intermittent southwestward shifts of the South Pacific Convergence Zone from its mean location northeast of New Caledonia. On inter-annual timescales, the occurrence of the rainfall states is modulated by El Niño Southern Oscillation (ENSO) events. The ENSO impact is strongest from mid-August to March with more (less) frequent trade regimes 1–2 and less (more) frequent unstable trade regime 4 and states 5–6 during central-Pacific warm (cold) ENSO events. Stochastic simulations of daily rainfall occurrence and amount at the 55 stations are generated by using predictors based on Niño 4 sea surface temperature index and a local intra-seasonal (15–80 days) OLR index superimposed on a climatological annual cycle. The cross-validated skill peaks in September–November.

**Electronic supplementary material** The online version of this article (doi:10.1007/s00382-015-2712-0) contains supplementary material, which is available to authorized users.

✉ Vincent Moron  
moron@cerege.fr

Renaud Barbero  
renaudb@uidaho.edu

Andrew W. Robertson  
awr@iri.columbia.edu

<sup>1</sup> CEREGE, UM34 CNRS, Aix-Marseille University, Aix en Provence, France

<sup>2</sup> IRI, Columbia University, New York, NY, USA

<sup>3</sup> Lamont-Doherty Earth Observatory, Palisades, NY, USA

<sup>4</sup> Department of Geography, University of Idaho, Moscow, ID, USA

**Keywords** Hidden Markov Model · Non-homogeneous HMM · Annual cycle · ENSO · Intraseasonal variability · Seasonal prediction

## 1 Introduction

New Caledonia (NC) is an archipelago in the subtropical SouthWest Pacific (20°S, 166°E). It comprises a NW–SE 400-km long main island, called ‘Grande Terre’ and small islands, including Loyauté islands, almost 50 km at the NE of Grande Terre. The main island is rather mountainous with a central range usually  $\geq 750$  m asl and two main peaks  $\geq 1600$  m asl, while the other smaller islands are lower. NC has a climate typical of many tropical and subtropical islands, being characterized by moderate to high temperatures and high humidity, and quasi-permanent Easterly trades all year round. Rainfall is less uniform as topographical effects cause significant variations between windward (i.e. east) and leeward (i.e. west) coasts (Barbero and Moron 2011; Lefèvre et al. 2010; Leroy 2006; Leroy and Céron 2007).

Due to its geographical location, NC is neither under the direct control of the Australian monsoon (Chang et al. 2005; Jourdain et al. 2013; Robertson et al. 2011; Wheeler and McBride 2005), which brings ample rainfall to Northern Australia, nor under the main axis of the South Pacific Convergence Zone (SPCZ) which is located at about 15° northeast of NC during austral summer (Hafke and Magnusdottir 2013; Matthews 2012; Vincent 1994; Widlansky et al. 2011). At the regional scale, NC comes under the influence of both the planetary-scale subsidence associated with South Pacific Hadley cell as well as intermittent southwestward displaced SPCZ. NC is also located close to the main cyclonic area in SW Pacific (Basher and Zheng 1995; Revell and Goulter 1986). The tropical cyclones (TCs) usually appear north of NC between the Coral Sea and Central Pacific, sometimes till French Polynesia, and then travel southward, eventually crossing NC. Some of them change into strong extratropical storm between NC and New Zealand such as Patsy in 1986 (Sinclair 1993). A total of 7 (in SE quadrant of NC) to 16 (in NW quadrant of NC) TCs have been recorded during a 20-year period from 1969/1970, so  $< 1$  TC per year in mean (Basher and Zheng 1995). The record of MétéoFrance [http://www.meteo.nc/cyclone/cyclones\\_passes?view=cyclones](http://www.meteo.nc/cyclone/cyclones_passes?view=cyclones) counts 20 TCs and 4 strong tropical depressions impacting NC from September 1, 1980 to August 31, 2010 (that is the period of this study), so a similar relative frequency to (Basher and Zheng 1995). Extratropical perturbations also play a minor role during Austral winter, due to the rather northward location of the subtropical Jet stream and its associated stormtrack at these longitudes (near 30°S at 300 hPa in July, Trenberth 1991; Vera 2003). The windward/leeward dipole is superimposed on these patterns and could switch from its usual E/W polarity when low-level westerlies replace temporarily usual trades.

All these phenomena exhibit considerable sub-seasonal and interannual-to-interdecadal variability. On interannual timescales, the relationships between NC rainfall and El Niño Southern Oscillation (ENSO) are the subject of numerous studies (Delcroix and Lenormand 1997; Fischer et al. 2004; Morlière and Rébert 1986; Nicet and Delcroix 2000). ENSO events also play a role in anomalous shift and/or intensity of the SPCZ, which can impact NC rainfall anomalies. Warm (cold) ENSO events tend to be related with an anomalous NE (SW) shift of the SPCZ (Folland et al. 2002; Vincent et al. 2011). In consequence, Morlière and Rébert (1986) showed that NC experienced a rainfall shortage during warm ENSO events (from April to May of the next year). Nicet and Delcroix (2000) found a correlation of 0.54 between low-pass filtered NC rainfall anomaly and Southern Oscillation Index at monthly time scale. Fischer et al. (2004), then Barbero and Moron (2011) showed that NC is far more sensitive to central Pacific (or Modoki) events than eastern Pacific ones. The difference between Eastern and Central events is stronger during the warm ones. The strongest ENSO response in NC rainfall is observed in Austral spring, mainly due to the interaction between the annual cycle of sea surface temperatures (SST) in equatorial central Pacific ( $SST \geq 29$  °C) combined with the zonal SST gradient related to ENSO events, which lead to a strong low-level convergence and associated latent heat release along the equator coupled with a strong subsidence anomaly around NC latitudes (Barbero and Moron 2011). It tends to delay the onset of wet season in NC and increases strongly the fire season across the archipelago (Barbero et al. 2011; Moron et al. 2013).

At intraseasonal time scales, the dominant mode of variability in the tropical atmosphere is the Madden–Julian oscillation (MJO, Madden and Julian 1971, 1994). It consists primarily of a large-scale deep convective anomaly propagating eastward from the Indian ocean to the dateline. Its time scale operates typically between 30 and 60 days. Matthews and Li (2005) showed that when deep convection is anomalously enhanced over Indonesia (corresponding to the phases 4–5 of the eight-phase composite of Wheeler and Hendon (2004), there is also increased (decreased) rainfall SW (NE) of the long-term main axis of the SPCZ, including NC, but the rainfall anomaly is modest there ( $\leq 1$  mm/day in CMAP gridded rainfall, Matthews and Li 2005). Leroy and Wheeler (2008) indicated that TC genesis locations tend to be clustered poleward and somewhat westward of the MJO's enhanced convective envelope, that is during phases 4–5 and 6–7 near Australia (between 135°E and 180°). In the tropical and equatorial portions of the SPCZ, variability indeed peaks between 30 and 60 days, but also around 2 weeks (Widlansky et al. 2011). At sub-monthly time scale ( $\leq 20$  days) as well as intraseasonal (20–200 days) one, a major mode of variation seems

to be associated with regional-scale atmospheric propagating anomalies perpendicular to the main axis of the SPCZ from SE Australia to sub-equatorial central Pacific (Matthews 2012). The main mechanism is the equatorward incursion of synoptic wave train from the subtropical stormtrack into the equatorial westerly duct over the central Pacific (Matthews 2012; Van Der Wiel et al. 2015). Negative zonal stretching deformation at 200 hPa (e.g. deceleration of zonal component of the wind with longitudes) may play a role in the enhancement of convection on the tilted axis parallel to the mean location of the SPCZ (Widlansky et al. 2011). These phenomena can impact NC rainfall anomaly at sub-monthly to intraseasonal time scale due to its location near the core of the western pole of the shifted SPCZ mode identified by Matthews (2012), Van Der Wiel et al. (2015).

The aim of this paper is to examine year-round variability of daily rainfall recorded on a network of stations across New Caledonia and relate this variability to the atmospheric circulation from daily to interannual time scales. This analysis is complementary to previous analyses of weather types (or regimes) around New Caledonia (Lefèvre et al. 2010; Leroy 2006). Weather types describe large-scale, persistent and recurrent atmospheric patterns. Around New Caledonia, (Lefèvre et al. 2010; Leroy 2006) found four main weather types in Austral summer (November–April) characterized by varying speed of low level trades and varying location of the subtropical anticyclone, while one weather type refers to SW shift of the SPCZ [referred as “Tropical” regime by Lefèvre et al. (2010)]. Our analysis starts from a discrete set of rainfall states defined using an Hidden Markov Model (HMM) throughout the calendar year, and is not restricted to austral summer as in (Lefèvre et al. 2010; Leroy 2006). Starting from local-scale rainfall offers also a distinct starting point from the regional-scale one provided by weather types. In this paper, we apply the HMM to 55 stations records of daily rainfall over NC over 30 years from September 1980 to August 2010. The rainfall datasets and its climatology are described in Sect. 2. The HMM is shortly presented in Sect. 3, then its application for rainfall occurrence and amount is detailed in Sect. 4 with the associated atmospheric variations at various time scales. Potential predictability of HMM states and rainfall are explored in Sect. 5. Section 6 provides a summary of the results.

## 2 Data and climatology

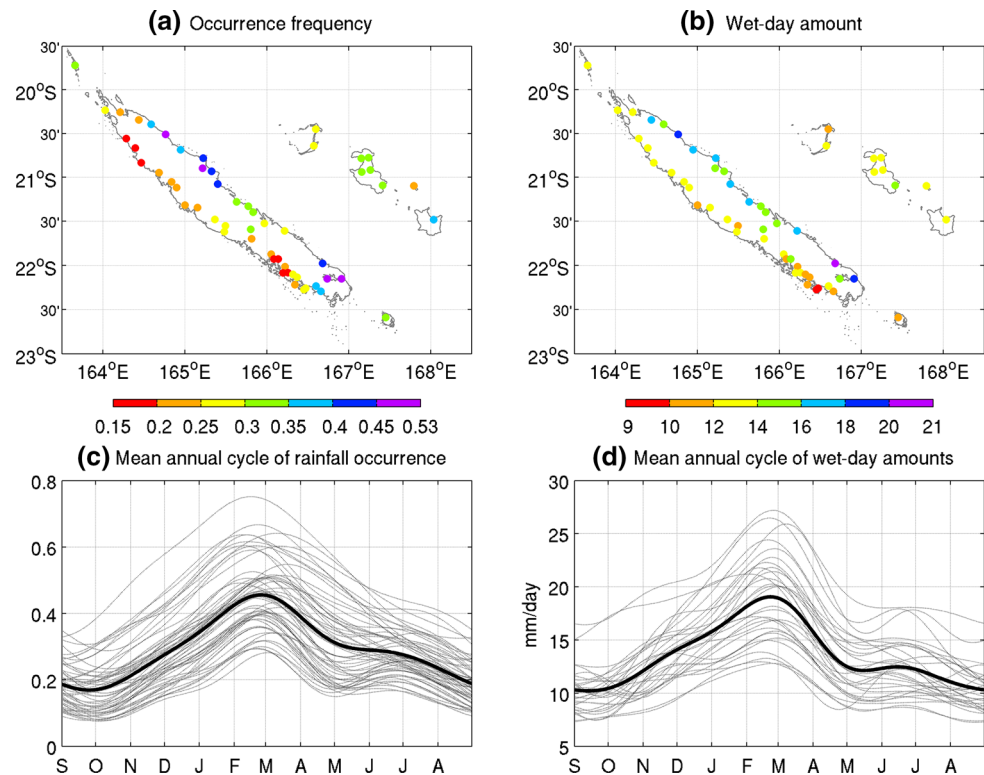
We use daily rainfall amounts at 55 stations over New Caledonia for the September 1–August 31 year, 1980–2010. Leap day amounts have been added to February 28. These data were obtained from MétéoFrance. There are 6.4 % of

missing entries. All computations of HMM and non-homogeneous HMM (NHMM, see Sect. 3) are made without any filling of these missing entries. However, the analysis of the potential predictability of intraseasonal characteristics of rainfall (in Sect. 5.2) needs a complete observed rainfall record. We have filled the missing entries with a NHMM using the leading Empirical Orthogonal Function (EOF) of daily rainfall as ‘predictor’ (see Sect. 3).

Figure 1 shows the locations of the 55 stations together with the climatological daily probability of rainfall occurrence defined as days receiving at least 1 mm and mean rainfall amount on wet days. Climatological rainfall occurrence is largest along the windward (i.e. east) coast, while rainfall is less frequent on the leeward (i.e. west) coast. There are two maxima along the windward coast, in the extreme southeast of the island, and also where the orientation of the coast veers northward. Geographical contrasts in wet-day amount between windward and leeward coast are clearer than for occurrence (Fig. 1). The mean seasonal variations in occurrence and wet-day amount increase from mid-December and stay at a relatively high level till early April. Both quantities decrease rather abruptly during April and then slightly decrease till the driest months (i.e. September–October). The time variation of mean amount is noisier, with highest mean intensity observed at the end of the wet season in February and March.

Figure 2 shows climatological mean of Mean Sea Level Pressure and 850 hPa winds (upper panels), outgoing long-wave radiation (OLR) and 200 hPa winds (lower panels) for the driest (i.e. August–October, left panels) and wettest (i.e. January–March, right panels) trimesters. Daily winds are extracted from the National Center For Environmental Prediction 2nd version reanalysis data (Kanamitsu et al. 2002) while the OLR is extracted from the interpolated daily dataset of Liebmann and Smith (1996). At low levels, trades blow almost all year along. In August–October, NC is under the direct influence of the eastern edge of the subtropical anticyclone centered over Australia and trades blow over the whole southern tropical belt at 850 hPa between 22°S and the equator. In consequence, SPCZ is weak while low OLR values south and southeast of NC, are related to extratropical storms. In upper troposphere, the subtropical jet stream is strong with fastest westerlies  $\geq 45$  m/s between 26°S and 30°S. It corresponds to the Australian subtropical Jet which acts as a waveguide for Rossby waves from Indian Ocean to Central and Eastern Pacific Ocean (Ambrizzi et al. 1995). In January–March, the subtropical anticyclone is shifted south of 26°S, while SPCZ is far stronger than in August–October. Subtropical jet stream is also slower (max. speed near 23 m/s and shifted just 2°S–3°S southward of its August–October’s latitude (Fig. 2).

**Fig. 1** Rainfall station locations and mean annual rainfall. *Dots* denote **a** the climatological daily rainfall probability of wet day receiving at least 1 mm (1980–2010) and **b** the corresponding wet-day amount. *Lower panels* show the mean annual cycle of **c** occurrence of wet days and **d** wet-day amount (mm/day) at each station (*dotted line*) with spatial average (*bold line*). In **c**, **d**, the daily mean is low-pass filtered with a recursive Butterworth filter with a cut-off at 1/90 cycle-per-day



### 3 The Hidden Markov Model

HMM provides a probabilistic framework of the joint distribution of daily rainfall at the network of 55 stations. Since this method has been extensively detailed in Robertson et al. (2004, 2006, 2009), only a short summary is given here. The rainfall model consists of a delta function to model dry days (receiving  $\ll 1$  mm of rain) and a mixture of two exponentials to describe rainfall amounts during wet days. The model is fitted using maximum likelihood via the expectation-maximization (EM) algorithm. Basically, the multivariate sequences of daily rainfall amounts for the network of 55 stations are assumed to be generated by a Markov chain of hidden weather states. The joint distribution is factorized as a square stochastic matrix of state transition probabilities. The HMM model assumes also that the daily rainfall for a given day depends only on the hidden state on that day, so that all rainfall autocorrelation is treated at the state level. The station components of the vector of rainfall amounts on any day are conditionally independent of each other given the hidden states (Robertson et al. 2004, 2006). Previous studies demonstrated that a mixture of two exponentials represents well the distribution of daily rainfall (Robertson et al. 2006; Wilks and Wilby 1999).

Input variables (predictors) are introduced into the HMM, by creating a non-homogeneous HMM (NHMM). In NHMM, the transition probabilities amongst states are

defined as a univariate or multivariate logistic function of predictor(s) input time series. NHMM is used here two times; (1) first, to get a complete rainfall database to compute intraseasonal quantities (used in Sect. 5.2). The four leading EOF of daily rainfall anomalies are used as predictors. Raw data are square rooted before the computation of normalized anomalies relatively to the long-term mean of each station. The missing entries were replaced by the daily mean climatological values before computing the four leading EOFs. This NHMM is not cross-validated. Note that using a simple univariate stochastic weather generator leads to similar results (not shown); (2) second, to analyse potential predictability of hidden states (see Sect. 5.1) and rainfall (see Sect. 5.2), three predictors are used. A first one is simply a replication of the same climatological annual cycle of rainfall defined as the spatial average of climatological daily rainfall of the 55 stations low-pass filtered with a recursive Butterworth filter with a cut-off at 1/90 cycle-per-day. A daily Niño 4 time series is computed by sub-sampling monthly time series. Lastly, an intraseasonal index (ISI, see Sect. 4.4) is used as a measure of the intraseasonal variability. We trained four different models; the first one considers annual cycle of rainfall only to check out the reproduction of annual cycle of HMM states. The second and third ones add respectively ISI and Niño 4 to annual cycle of rainfall respectively and the last model includes the three predictors to specify the states. The

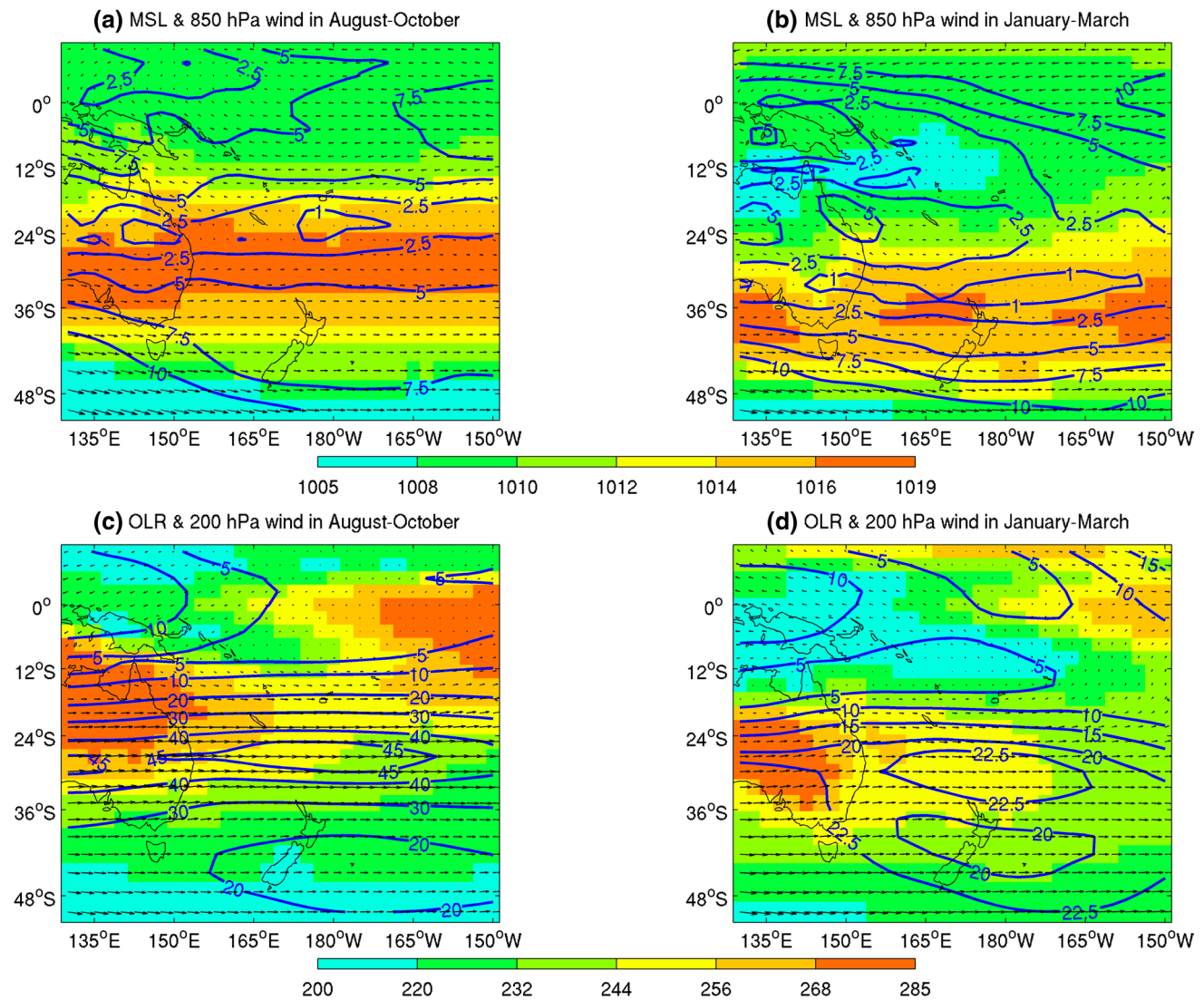


**Fig. 2** Climatological mean of 850 hPa winds (vector and speed in m/s in blue contour) and mean sea level pressure (shadings in hPa) in **a** August–October and **b** January–March. Climatological mean of

200 hPa winds (vector and speed in m/s in blue contour) and outgoing longwave radiation (shadings in W/m<sup>2</sup>) in **c** August–October and **d** January–March

learning stage is cross-validated with parameters trained on 25 years and the last 5 years are blindly simulated from these parameters. This is repeated 6 times to get a daily sequence of HMM states given one, two or three predictors. The NHMM is computed on 50 replicates and 100 simulations are made.

#### 4 HMM states of daily rainfall and associated atmospheric circulation

##### 4.1 The choice of number of states

As in Robertson et al. (2004, 2006, 2009), cross-validation is used to evaluate the quality of the fitted HMMs by

maximizing the log-likelihood of the parameters learned during the training period of 25 years, given the observed rainfall of the remaining 5 years. So 5 years are iteratively removed, the model is trained on the remaining 25 years and the simulations compared with observed rainfall for the six 5-year validation periods. In each case, the EM algorithm was run 50 times from different initial seeds and the run with the highest log-likelihood is selected. The normalized out-of-sample values of the log-likelihood are plotted in Fig. 3 for 2–10 states. As found elsewhere (Robertson et al. 2004, 2006, 2009), the out-of-sample log-likelihood of the models increases monotonically with the number of states in an asymptotic manner. This is expected since a simple model of only 2–10 states is considerably simpler than the true rainfall variations at daily time scales. There

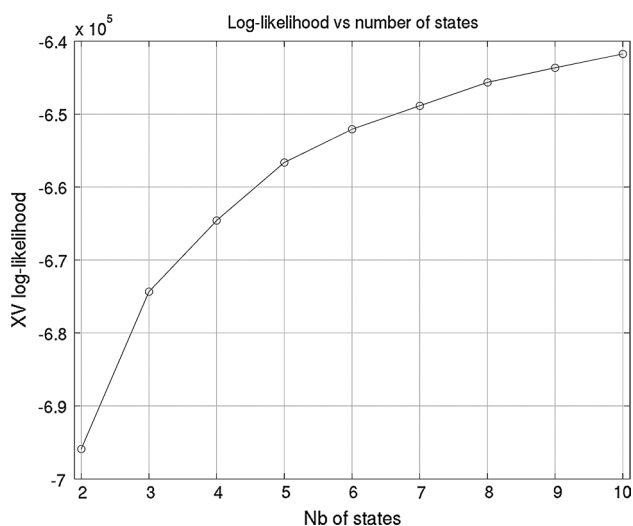


**Fig. 3** Out-of-sample log-likelihood for amounts model using mixture of two exponential distributions for rainfall on wet days. The HMM is trained on 25 years and cross-validated on the remaining 5 years

is always a balance between the degree of (out of sample) fit and the parsimony of the model which is usually desired for diagnosis and prediction purposes. Here, we choose 6 states. The results discussed below are not sensitive to choosing between 5 and 8 states.

#### 4.2 The six-state model parameters

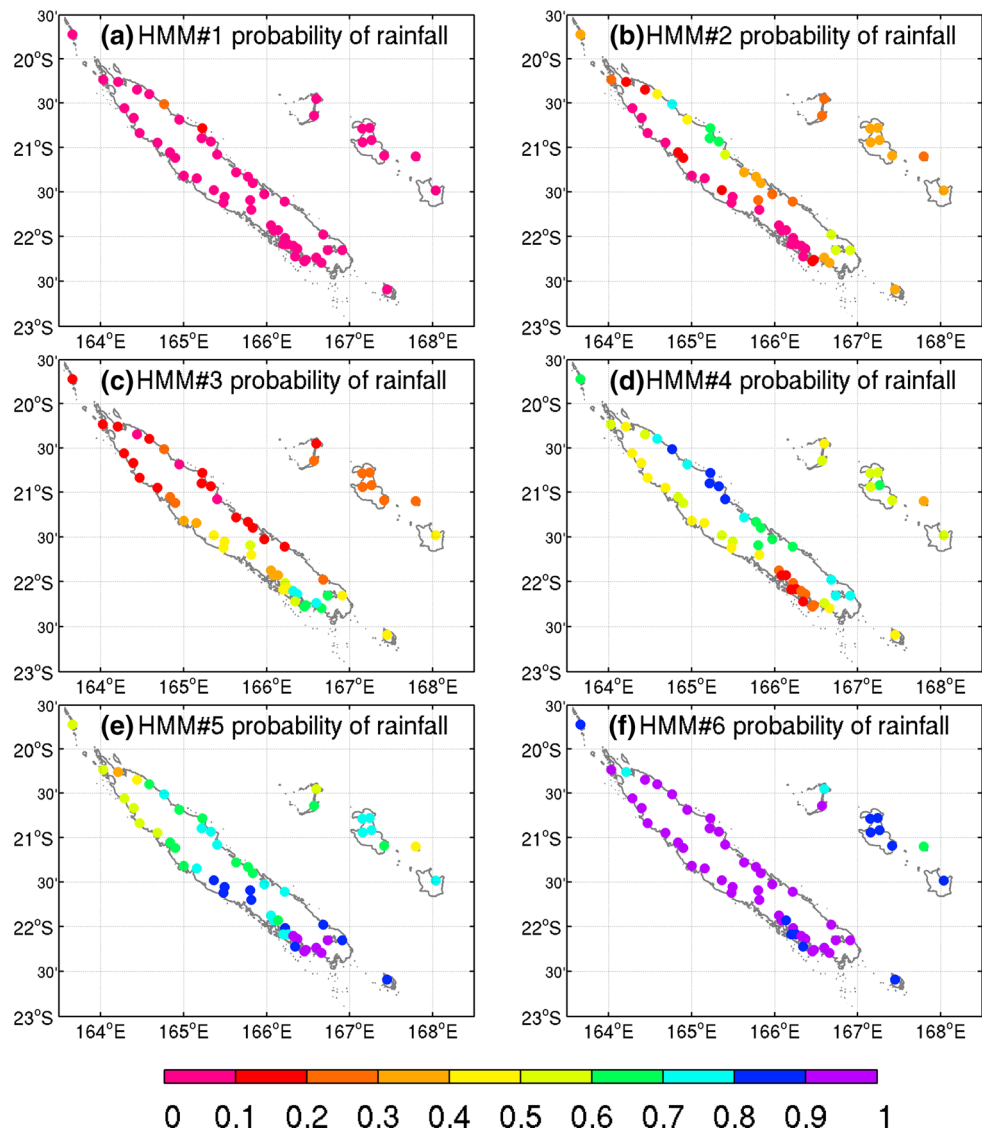
Having chosen the six-state model, its parameters were estimated from the entire 10,950-day rainfall record without cross-validation. The EM algorithm is restarted 50 times selecting the run with the highest log-likelihood. The resulting rainfall parameters are illustrated in Fig. 4 in terms of the probability of rain and in Fig. 5 in terms of mean rainfall amount on wet days. The latter was computed from the parameters of the mixed exponential distribution. States are ordered according to the rainfall probability spatially averaged over the 55 stations.

State 1 is by far the most frequent and the most persistent state (Table 1). It is a very dry state (Figs. 4a, 5a). States 2–4 show some clear E–W dipolar patterns (Figs. 4b–d, 5b–d). These states share also a weak persistence with state 6 (Table 1). Between 85 and 93 % of spells last <3 consecutive days (Table 1). State 4 shows frequent and moderate rainfall along the windward coast while rainfall are less frequent and rather light (<10 mm in mean) along the leeward coast, especially in its southern part (Figs. 4d, 5d). State 3 shows light rainfall almost restricted to the southern part of the leeward coast. State 2 displays the same windward/leeward contrast as state 4 but rainfall frequencies and amounts are overall weaker.

State 6, the wettest state, exhibits large rainfall amounts everywhere (Figs. 4f, 5f). Even though it occurs rarely (<20 days per year), it accounts for almost 50 % of rainfall across NC. Note that it occurs far more frequently than tropical cyclones (<1 per year). State 5 is also rather wet, especially in the south of the main island, but mean wet-day amounts are far weaker than for state 6 (Figs. 4e, 5e). Together with state 6, both states occur for <15 % of time while they contribute to almost 70 % of total rain (Table 1). In fact, the states 5 and especially 6 include the most powerful TCs. The relative scarcity of TCs and tropical depressions and their different tracks ([http://www.meteo.nc/cyclone/cyclones-\\_passes?view=cyclones](http://www.meteo.nc/cyclone/cyclones-_passes?view=cyclones)) precludes their straightforward identification with a specific state. Both states show the same seasonality with a weak peak in mid-February and early March (Fig. 6), which corresponds to the annual peak of rainfall frequency and amount in NC. Of the 34 days categorized as TC according to MF [http://www.meteo.nc/cyclone/cyclones-\\_passes?view=cyclones](http://www.meteo.nc/cyclone/cyclones-_passes?view=cyclones), 23 (respectively 7) occur in state 6 (respectively 5). Moreover state 6 includes the wettest TCs impacting NC: the rainfall spatially averaged over the 55 stations equals 79 mm for the 23 events and only 15 mm for the 7 ones categorized in state 5. Removing the 23 TC days from state 6 (plus the day of strong tropical depression) from the total 582 days (Table 1) decreases the spatial average to 34 mm for the remaining 558 days of state 6. It suggests that the extreme wetness of state 6 (Fig. 5f) is somewhat exaggerated by a few tropical cyclones, but its non-TC days are still far wetter than the non-TC days of state 5 (spatial average of rainfall = 10 mm in state 5 vs 34 mm in state 6). Thus overall, state 6 may be interpreted as an intensified state 5 beyond the inclusion of the wettest tropical cyclones.

The state-transition is given in Table 2. The Markov property of the HMM is clear in the relatively large self-transition probabilities, i.e. persistence. State 1 and 2 are the most persistent. These state-transitions are of course consistent with the length of spells shown in Table 1. The most-probable sequence of the six states over the 30-year period has been estimated using the Viterbi algorithm as in Robertson et al. (2004). The average annual cycle is plotted in Fig. 6. The dry state 1 dominates from mid-May to mid-December, that is around the cool and dry Austral winter season. It still occurs almost 10 % of time in February during the core of the warm wet season. State 3 is unique with a relative peak during the Austral summer. States 4–6 have similar seasonalities and become more prevalent around the Austral summer even if their frequencies are not null all year around. Note that the peak of the wettest state 5–6 coincides with the peak of annual rainfall in late February–early March. State 2 is rather constant between 20 and 35 % of times with two weak peaks on each sides of the annual peak of rainfall (Fig. 6).

**Fig. 4** Occurrence probabilities of wet days receiving at least 1 mm for the six-states HMM rainfall parameters



We explore the changes in rainfall state due to annual cycle by plotting the mean probability and mean amount of wet days at monthly time scale (Fig. 1, Supplementary Information—SI hereafter). The mean probability are rather constant across the year without any clear signal at annual scale (Fig. 1 SI, left column). There are small changes in mean amount (Fig. 1 SI, right column) with slightly larger rainfall amounts during wet season, between November and April. It is especially marked for state 4 with spatially-averaged mean rainfall  $\geq 10$  mm between November and April and  $\leq 7$  mm in July–August. The annual modulation is less clear for the wettest states 5–6, especially the last one. In summary, annual cycle has almost no impact on mean probability of rainfall and only a weak impact of mean amount of rainfall associated with the states.

### 4.3 The atmospheric conditions

Composites of atmospheric circulation variables are plotted for each state in Fig. 7, computed by averaging over the days assigned to each state by the Viterbi algorithm. State roses of 850 hPa winds spatially averaged over 4 grid-points over NC are plotted in Fig. 8. Note that any other level between 1000 and 700 hPa leads to similar results (not shown).

NC is directly under the eastern edge of a large anticyclonic circulation centered over Australia (Fig. 7a) with a regional-scale subsidence at 500 hPa (not shown) in state 1 which is rather similar to the climatological mean of August–October (Fig. 2a). Dominant low level ESE–SE trades are usually weak (Fig. 8a). This state is predominant outside the core of the wet season. In state 2, the low-level

**Fig. 5** Wet-day amount during wet days receiving at least 1 mm for the six-states HMM rainfall parameters

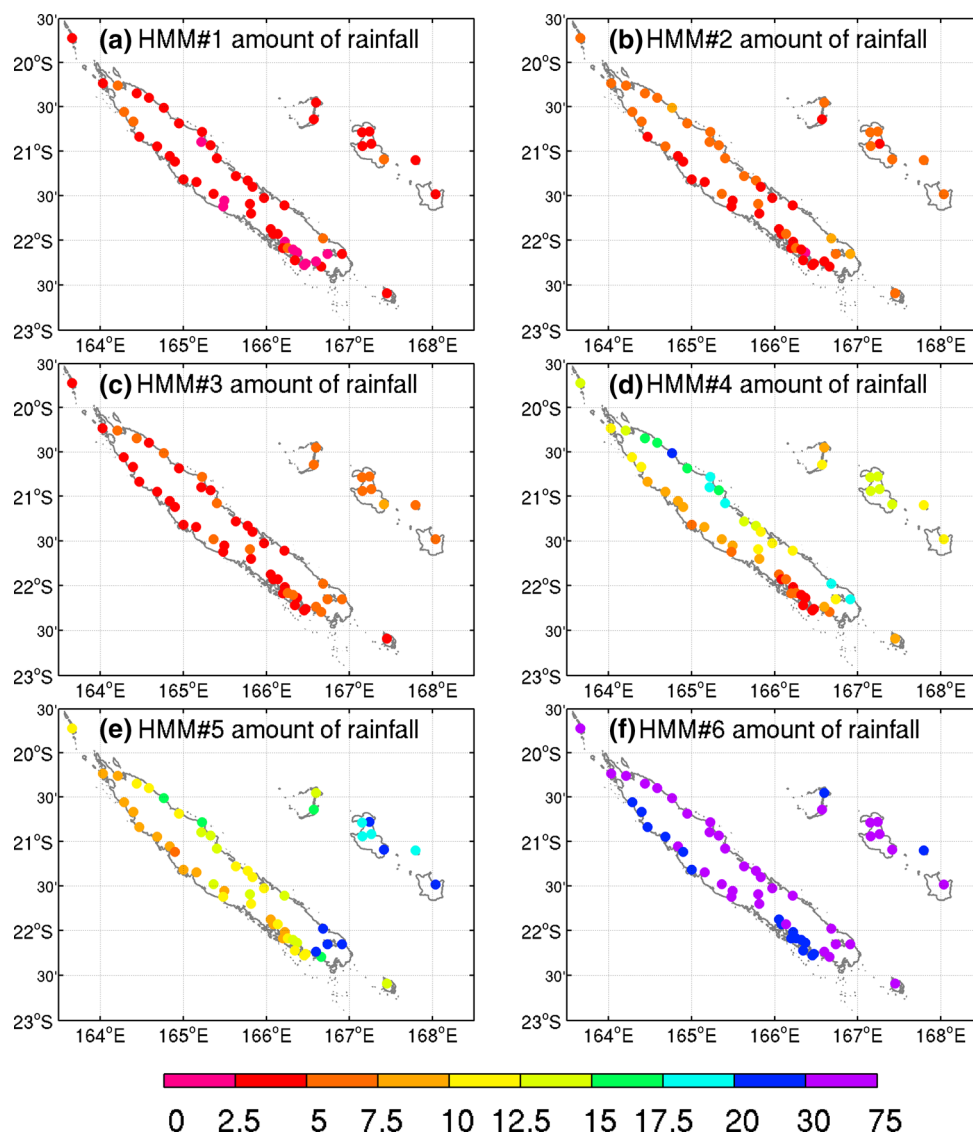


**Table 1** (2nd column) Total number, (3rd column) percentage of HMM states with their contribution to total rainfall (4th column) in mean and (5th column) standard deviation computed across the 55 stations (September 1980–August 2010)

State	Number	Frequency	Mean	SD	Spells (3 days)	Days (3 days)	Spells (5 days)	Days (5 days)	Spells (7 days)	Days (7 days)
HMM1	3957	36	0.01	0.01	46.1	76.8	22.1	51.2	11.0	32.6
HMM2	2932	27	0.08	0.05	27.0	54.5	8.6	24.9	2.5	9.4
HMM3	1177	11	0.05	0.04	10.1	24.5	1.3	4.5	0	0
HMM4	1363	12	0.17	0.08	14.6	33.5	1.7	6.7	0.5	2.4
HMM5	939	9	0.21	0.07	6.5	16.3	0.6	2.2	0	0
HMM6	582	5	0.47	0.08	13.3	30.4	2.5	8.8	0	0

The columns 6–11 give the percentage of spells and days included in consecutive days having the same HMM states and lasting respectively at least 3, 5 and 7 days. The longest spell for HMM 1–6 lasted respectively 22, 14, 6, 11, 6 and 6 days

anticyclonic circulation (positive relative vorticity in the southern hemisphere) and associated regional-scale subsidence is shifted southeastward with a closed anticyclonic

pattern between NC and New Zealand (Fig. 7b). E trades are faster than in state 1 (Fig. 8b). State 2 is rather similar to regime 1 of Lefèvre et al. (2010) and it leads to light

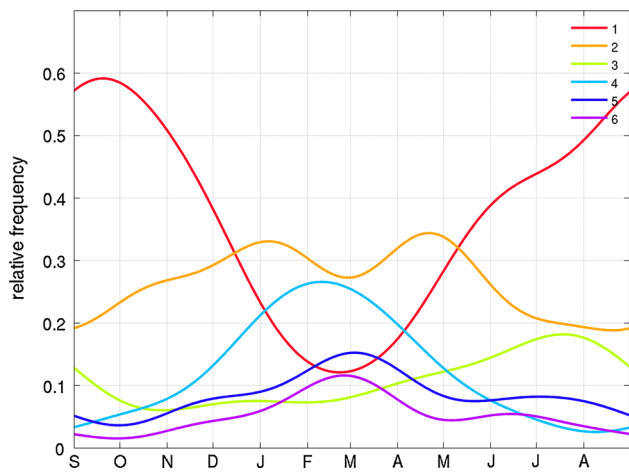


**Fig. 6** The mean annual cycle of HMM state occurrence computed from the estimated daily sequence. The daily frequency is low-pass filtered with a recursive Butterworth filter with a cut-off at 1/90 cycle-per-day

rainfall on the windward coast while the leeward coast remain almost absolutely dry. State 4 is rather similar to state 2 (Fig. 7d) except that ascending motions are observed at 500-hPa over NC (not shown). Trades blow dominantly from ENE to ESE and wind speeds are close to the mean climatology (Fig. 8d). The remaining 3 states show more cyclonic conditions (negative vorticity) over or near NC (Fig. 7c, e, f). State 3 shows a clear extratropical trough axis east of NC. This state may be related to extratropical perturbations traveling south of NC and local rainfall in the southwestern part of the island could be easily associated with post-cyclonic cold fronts (Fig. 7c). Low level winds come usually from SW quadrant and they are faster than climatological winds (Fig. 8c). State 5 and 6 are associated with similar patterns in low troposphere, but with larger amplitude in state 6 than in state 5. State 5 shows an elongated cyclonic vorticity axis stretched from New Guinea to NC with strong northerlies toward NC. The SPCZ tends to be southwestward shifted relatively to its climatological location (Fig. 7e). Low level winds show a weak over-representation of northerlies relative to climatology even if

ESE–ENE trades are still the most frequent (Fig. 8e). State 6 shows a closed cyclonic center between Australia and NC and the SPCZ is even more southwestward shifted than in state 5 (Fig. 7e, f). The southward moisture advection from sub-equatorial western Pacific across NC is far stronger in state 6 than in state 5 with fast northerlies (Fig. 8f). So despite their similarity, both states 5 and 6 can not be simply considered as two stages of a traveling wave since the transition among them is rather weak with no preferred direction (Table 2). There are both close to the “tropical” regime of Lefèvre et al. (2010).

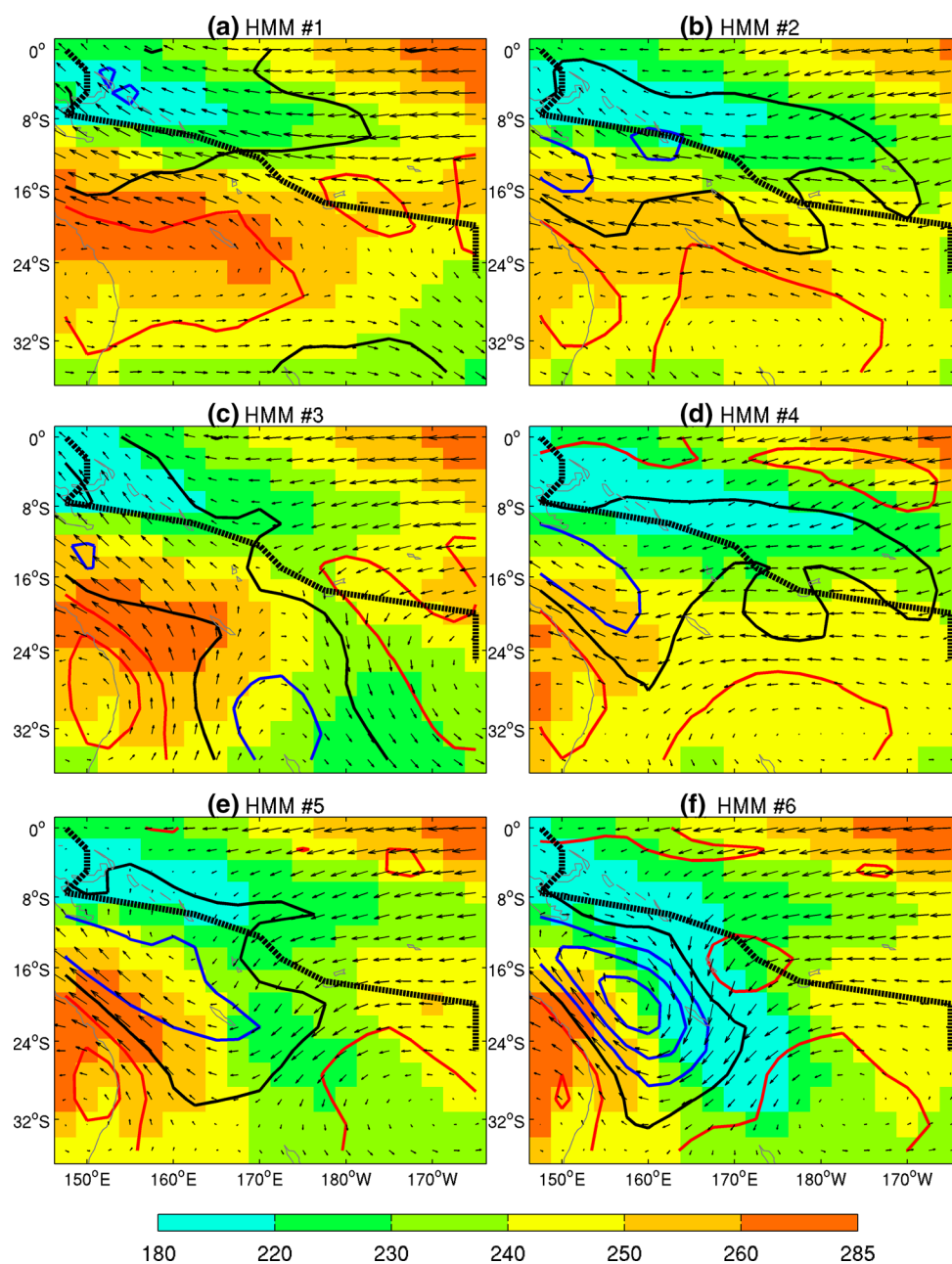
Figures 2 and 3 of SI display the atmospheric composites associated to each state restricted to August–October and January–March respectively. It helps to diagnose the impact of annual cycle on the atmospheric composite associated with each state. A band of 850 hPa cyclonic vorticity is systematically stretched south of the ITCZ–SPCZ in January–March (Fig. 3 SI). This quasi-constant feature changes obviously the atmospheric composites associated with each state. It is especially marked in states 3, 5 and 6. In August–October, state 5, and even state 6, tends to the pattern of state 3, with low OLR values shifted south of the mean values (Fig. 2 SI). On the contrary, state 3 in January–March tends to the pattern of states 5–6 observed in mean (Fig. 3 SI). Such changes are expected due to the large variance conveyed by the annual cycle, but it suggests also that quasi-constant rainfall states (Fig. 1 SI) could be related to different atmospheric pattern. Figure 4 of the SI is the same as Fig. 8 of the main text except that wind roses are shown for each state in August–October and January–March. As suggested by the atmospheric composites, the trade states (i.e. states 1, 2 and 4) are rather stable with the same main angle (ESE in states 1 and 2, ENE in state 4, Fig. 4 SI), even if there are changes in the relative frequencies of sub-divisions of the low level easterlies. There are more changes in cyclonic states 3, 5 and 6. State 3 is associated with W–SW low level winds, typical of extratropical cold fronts, in August–October, while it is more frequently associated with South Easterlies in January–March, in association with the location of NC SE of a main cyclonic pole (Fig. 3 SI). The fact that winds are

**Table 2** Probability of transition from (in row) to (in column) the HMM states

	HMM1	HMM2	HMM3	HMM4	HMM5	HMM6
HMM1	<b>0.69</b>	0.23	0.30			
HMM2	0.15	<b>0.53</b>	0.12	0.28	0.18	0.15
HMM3	0.11		<b>0.33</b>		0.10	
HMM4		0.13		<b>0.37</b>	0.22	0.26
HMM5			0.14	0.16	<b>0.26</b>	0.14
HMM6					0.15	<b>0.38</b>

For clarity, the empty cell indicate a probability smaller than 0.10 and the self-transitions are indicated in bold face

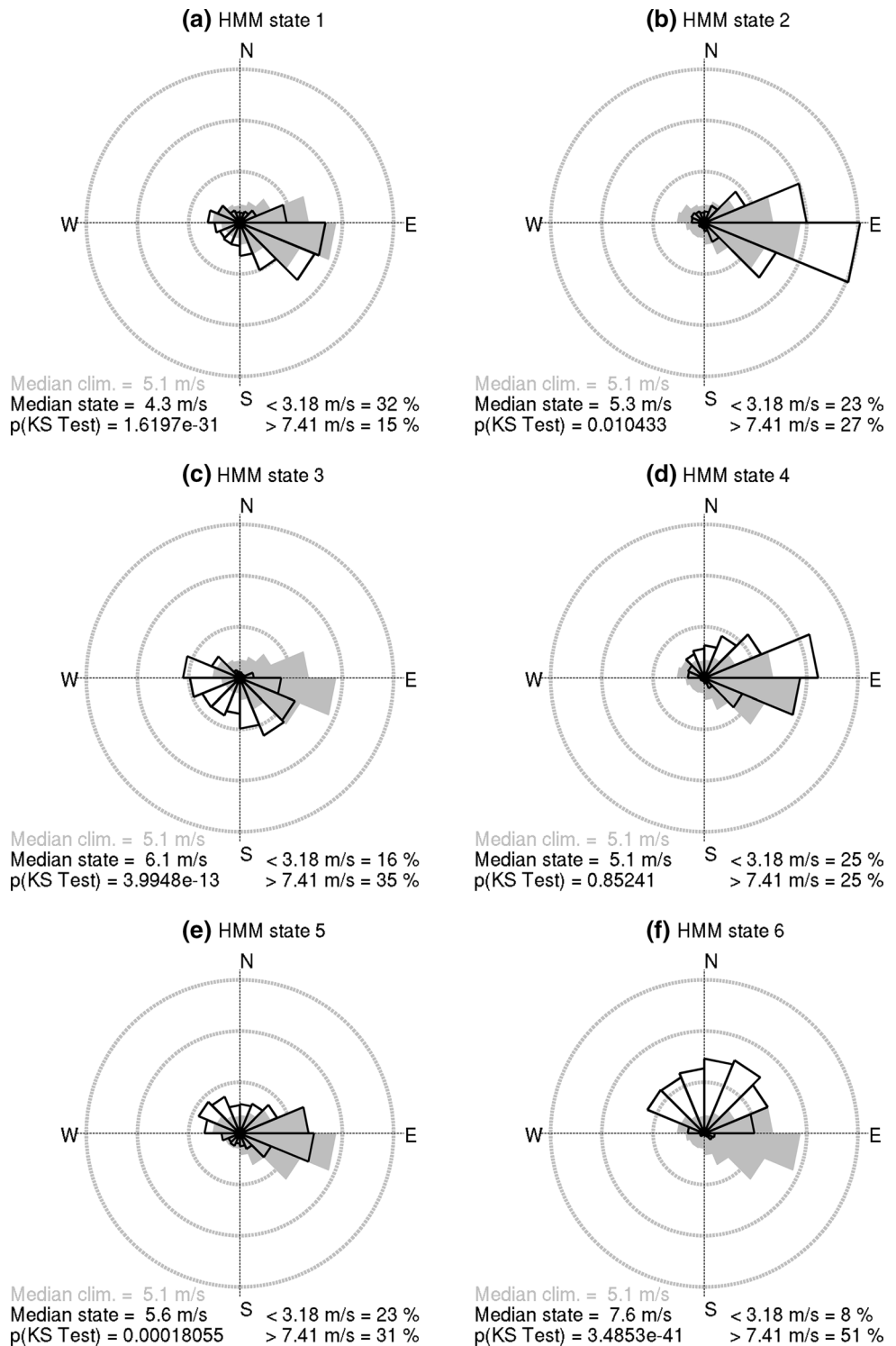
**Fig. 7** Composites of moisture flux vertically integrated from the surface to 700 hPa (*vector*) 850 hPa relative vorticity (*black line* is zero. Negative-cyclonic-values in *blue* with *contour* interval of 0.25 m/s). Positive-anticyclonic-values in *red* with *contour* interval of 0.25 m/s), and outgoing longwave radiation (*shadings* in  $\text{W/m}^2$ ). All composites are total fields, computed from unfiltered daily data. Relative vorticity is computed as the curl (i.e. rotational) of the horizontal winds at 850 hPa using a centered difference approach (MATLAB function curl). The mean location of SPCZ (*dashed black line*) is estimated as the minimum mean OLR by latitude



southerly in both cases is important since the mean rainfall spatially-averaged over NC is moderately correlated with meridional component of the 850 hPa winds averaged over the grid-points including NC (see caption of Fig. 8) ( $-0.40$  for the frequency and  $-0.49$  for the mean amount for wet stations) while the correlations is close to zero for the zonal component of 850 hPa wind. State 5 shows the most unstable wind rose with dominant westerlies in August–October, similar to state 3 in that season, while it is associated with clear easterlies in January–March. State 6 shows also some variations, but winds blows from the north in both seasons conveying moist air from subequatorial latitudes to NC (Fig. 4 SI).

Composite anomalies of vertically-integrated moisture flux, OLR and 850 hPa vorticity relative to the mean annual cycle are plotted for the 6 states in Fig. 9. Only statistically significant moisture flux anomalies (zonal or meridional components) and OLR at the two-sided 99 % level according to a Student's  $t$  test are plotted. The significant anomalies cover a larger equatorial area in state 2 (Fig. 9b), and 6 (Fig. 9f), which are broadly out-of-phase. Such significant anomalies are also visible in state 4 (Fig. 9d), while the other states tend to show significant anomalies confined to subtropical latitudes. More precisely, state 1 shows a clear anticyclonic anomaly between Queensland and NC decreasing low level trade winds by superimposing a SW

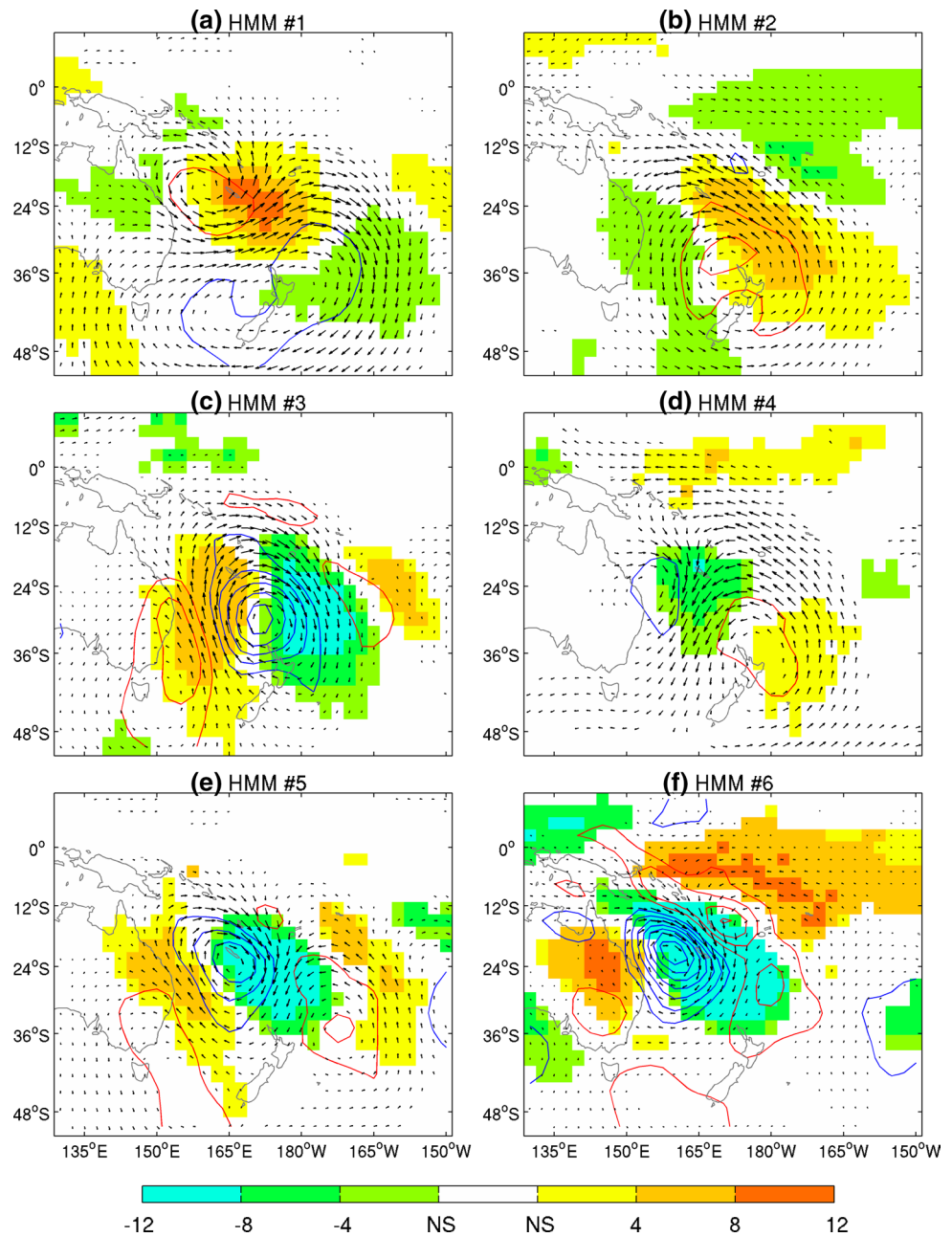
**Fig. 8** Wind rose of the directions (divided in 16 equal angles) of the spatial average of 850 hPa winds between 163.75°E–168.75°E and 18.75°S–23.75°S in mean (gray shading) and for each state (black contour). The directions are expressed as relative frequency versus the total number of days and the three gray circles indicate relative frequencies of 10, 20 and 30 %. The median wind speed (in black vs. the median of full PDF in gray) as well as the *p*-level of the Kolmogorov–Smirnov test—KS test—(null hypothesis: the PDF of each state is equal to the full PDF) is indicated with the percentage of daily wind speeds under 3.18 m/s (=25 % percentile of the full PDF) and over 7.41 m/s (=75 % percentile of the full PDF)



anomaly on the climatological trades (Fig. 9a). This is consistent with weak low level raw winds over NC (Fig. 8a), canceling the windward/leeward opposition and generalizing dry conditions across NC (Figs. 4a, 5a). State 2 shows suppressed (enhanced) convection SW (NE) of the climatological axis of the SPCZ, consistent with a NE shift of

the SPCZ and/or its merging with equatorial ITCZ. This is associated with an anticyclonic anomaly centered NW of New Zealand (Fig. 9b). Low level trades are now reinforced with ESE anomalies over NC (Fig. 8b). State 3 is clearly associated with a closed cyclonic anomaly located between New Zealand and NC, associated with a zonal

**Fig. 9** Anomaly composites of vertically-integrated moisture flux from the surface to 700 hPa (vectors), OLR (shadings) and 850 hPa vorticity (red line: positive anomaly from 0.1 m/s, blue line negative anomaly from -0.1 m/s. Interval is 0.1 m/s). The anomalies are computed as daily anomalies relatively to the mean annual cycle and averaged for days assigned to each state. Moisture fluxes are displayed only when anomalies of either the zonal or meridional components is significant at the 99 % level according to a Student's *t* test, while shadings indicate OLR significant at the 99 % level according to a Student's *t* test



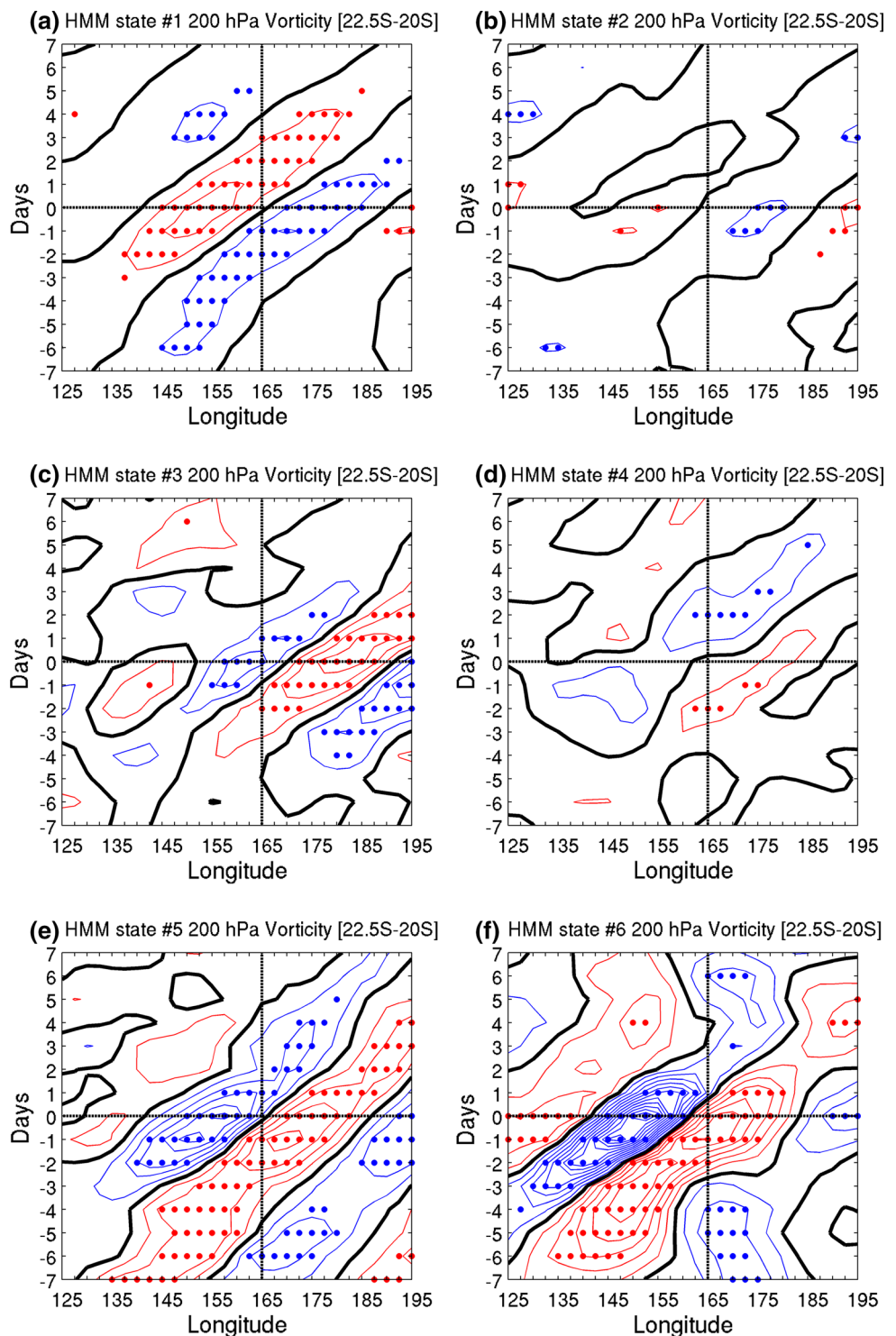
tripolar pattern of alternating OLR anomalies (Fig. 9c). State 4 shows strong southward anomalies of the moisture flux related to a NW–SE pair of cyclonic/anticyclonic anomalies between Queensland and New Zealand (Fig. 9d). State 5 shows a clear zonal wave train tilted perpendicular to the mean location of the SPCZ. A main cyclonic anomaly is located just over NC. This cyclonic anomaly is slightly displaced westward in state 6 and the zonal wave train is less obvious than in state 5 (Fig. 9e, f).

Figures 5 and 6 of SI display the composite atmospheric anomalies associated to each state restricted to August–October and January–March. The pattern is very similar for states 1, 3 and 5. The spatial patterns are also similar

in state 6 with larger OLR anomalies in January–March than in August–October, especially over the central equatorial Pacific. In state 2, the anticyclonic anomaly at 850 hPa is shifted southeastward in August–October than in January–March, but NC is under increased ESE winds in both seasons (Figs. 5, 6 SI) as for the mean pattern (Fig. 9b). The anomaly composites differ in state 4 at least for OLR and 850 hPa vorticity but NC stay under WNW anomaly at 850 hPa in both seasons (Fig. 9d).

Figure 9 shows a clear wavetrain associating 3 alternating poles on an E–W axis in state 3, and on a tilted NW–SE axis, almost perpendicular to the climatological location of the SPCZ, in state 2, 5–6. It suggests an active role of

**Fig. 10** Longitude-time composites from day  $-7$  to day  $+7$  of 10-day high-pass filtered 200 hPa vorticity averaged between  $23.75^{\circ}\text{S}$  and  $18.75^{\circ}\text{S}$  (blue cyclonic, red anticyclonic, black 0. Interval is  $0.05\text{ m/s}$ ). Blue and red dots indicate significant values at the 99 % level according to a Student's  $t$  test. The vertical dashed line is the approximate longitude of NC



transient synoptic wave in the occurrence of the associated states. Figure 10 displays time-longitude diagram of the high-pass filtered ( $\leq 10$  days) vorticity at 200 hPa over latitudes and longitudes including NC. Eastward propagating wave is clear for states 1, 3 and 5–6 with the largest amplitude observed for the last wettest state (Fig. 10f). The approximate zonal phase speed equals  $40^{\circ}$  in 6 days

( $=5-6\text{ m/s}$ ) while the zonal wavelength is close to  $40^{\circ}-45^{\circ}$ , i.e. wavenumber 9, consistent with a synoptic Rossby wave. There is no clear meridional propagation on latitude–time plots similar to Fig. 10 except that high-pass filtered vorticity is averaged between  $163.75^{\circ}\text{E}$  and  $168.75^{\circ}\text{E}$  and analyzed through time and latitude, while the largest amplitude is observed between  $25^{\circ}\text{S}$  and  $30^{\circ}\text{S}$  (not shown),

that is almost along the core of the Australian subtropical Jet (Fig. 2). The eastward propagating synoptic wave is far weaker for states 2 and 4 (Fig. 10b, d). So the apparent wavetrain seen in Fig. 9b, for state 2, should be related to a stationary atmospheric feature. Figure 7 in SI shows the same time-longitude composite for high-pass filtered vorticity at 850 hPa. A similar wavetrain appears at this low level for states 1, 3, 5–6 without any clear vertical tilt, suggesting an equivalent barotropic wave. State 1 occurs mostly during the anticyclonic phase. State 3, and states 5–6 occur in the center and respectively just at the beginning of the cyclonic phase travelling over NC (Fig. 7 SI).

#### 4.4 The relationships with ENSO and intra-seasonal variability

We next analyze ENSO modulation of HMM state occurrence frequency. Figure 11 shows the running correlations between Niño 4 SST index (defined from weekly SST dataset (Reynolds et al. 2002)) and the state occurrence frequency on sliding 12-week. The largest correlations are observed from October to February, especially during the first half of this period when more (less) states 1–2 (4–6) should be linearly related to warm ENSO events. State 3 is also positively related to Niño 4 in July–August but negatively around January. The correlations tend to vanish from mid-May to July–August, except for state 4 which still tends to be more (less) frequent during cold (warm) ENSO

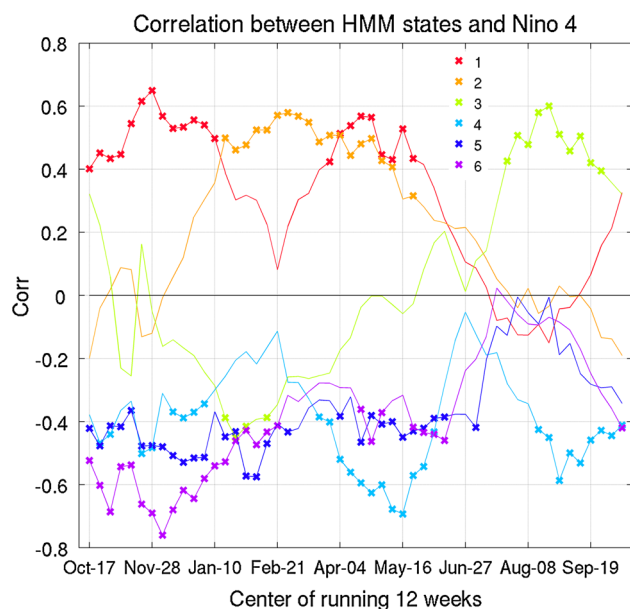


**Fig. 11** Running correlations between the Niño 4 box ( $160^{\circ}\text{E}$ – $210^{\circ}\text{E}$ ,  $5^{\circ}\text{N}$ – $5^{\circ}\text{S}$ ) and the frequency of HMM states on sliding 12-week windows. The crosses indicate significant correlations at the two-sided 95 % level of significance according to a random-phase test (Janicot et al. 1996)

events (Fig. 11). We explore the changes in state structure during warm and cold ENSO events. Figure 8 of SI shows the mean probability and mean amount during wet days  $\geq 1$  mm for warm and cold ENSO events. It suggests that ENSO does not impact the mean probability of wet days in each state since the distribution of anomalies between lower and upper quartiles matches almost perfectly between warm and cold ENSO events. The distribution in mean amounts is less similar but the differences between warm and cold ENSO events are not systematic across the states. In summary, it suggests that ENSO does (does not) impact on the frequency (mean pattern) of states.

At sub-seasonal time scales, many inter-related factors may affect HMM state occurrence. We first explore whether phase locking with the eight MJO phases as defined by Wheeler and Hendon (2004) might be present. The contingency between MJO phases and the six HMM states reveal rather weak anomalies (not shown) peaking for state 6 which occurs significantly less frequently than expected during MJO phase 1 ( $-38\%$ ) and 2 ( $-34\%$ ) respectively and more frequently in MJO phase 5 ( $+40\%$ ). The other anomalies do not reach 29 % in absolute value for state 2 and 3 and reach 20 % at maximum in absolute values for the remaining HMM states 1, 4 and 5. These overall weak anomalies are not surprising considering that planetary-scale MJO defined by Wheeler and Hendon (2004) reaches its highest amplitude between  $15^{\circ}\text{S}$  and  $15^{\circ}\text{N}$  in austral summer (Wheeler and Hendon 2004) and that (Matthews and Li 2005) indicated also that MJO signal, defined as the first EOF of intraseasonal OLR variability over the whole tropical belt is not significant over the CMAP grid-point corresponding to NC. The largest MJO signal is indeed shifted along the main axis of the SPCZ and on the western equatorial Pacific. We thus construct an intraseasonal index targeted on NC, defined by the band-pass filtered (15–80 days) OLR anomalies firstly spatially-averaged over  $161.25^{\circ}\text{E}$ – $168.75^{\circ}\text{E}$ ,  $23.75^{\circ}\text{S}$ – $18.75^{\circ}\text{S}$  box (Fig. 9, SI). This OLR index shows a larger amplitude around Austral summer and is also modulated at interannual time scale, partly in association with ENSO events (larger amplitude in cold ENSO events) and is not linearly related to planetary-scale MJO. This index has the advantage to focus on intraseasonal variations over NC and thus maximizes the potential link with rainfall, although it may be less predictable than planetary-scale MJO index. We return to this issue in the next subsection. To evaluate the potential effect of this intraseasonal index (ISI hereafter) on the modulation of HMM states, we computed 8 phases using the angle between this index and its derivative following (Moron et al. 1998). As for the case of the MJO index, the largest impact of ISI is observed for state 6 with strong positive anomaly in phase 3 ( $+200\%$ ) and negative ones ( $\leq 75\%$ ) in phases 6–8. The anomalies are weaker

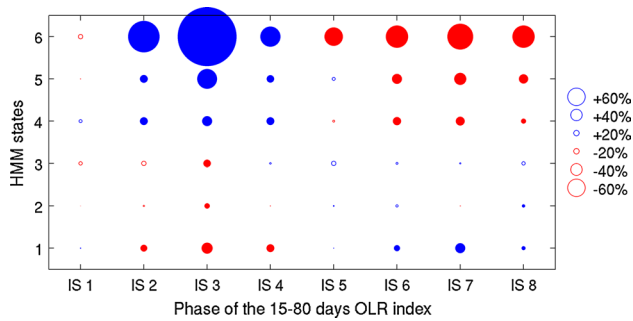


**Fig. 12** Anomalous probability of each HMM frequency estimated as the deviations from the expected frequencies during the eight phases of intra-seasonal variability (15–80 days) of an OLR index (=spatial average of 15–80 day bandpass OLR anomalies over 161.25°E–168.75°E, 23.75°S–18.75°S box, Fig. 9 SI). The filled red (blue) dots indicate significant negative (positive) anomalies at the two-sided 95 % level according to a random permutation (1000 times) of the yearly sequence of HMM

but in phase for states 4 and 5 (Fig. 12). States 1–3 show a reversed modulation to states 4–6 but the anomalies are usually  $\leq 25\%$ .

## 5 Potential predictability

### 5.1 HMM states

The potential predictability of state occurrence is tested using an NHMM with 3 predictors as explained in Sect. 3. Figure 13 shows the cross-validated skill of the state frequency by the 4 models. The daily occurrence is smoothed by a running 11-day window to enhance the intraseasonal, annual and interannual components which are assumed to be potentially predictable and reduce the synoptic and shorter time scales. Unsurprisingly, the skill reaches a maximum level for model 4 (all three predictors) except for states 1 and 5 and the skill is significant except for wintertime state 3 (Fig. 13a). This failure could be related to a myriad factors, but at least by its weak annual cycle and its weak modulation by either Niño 4 or ISI. The middle panel of Fig. 13 shows the skill at interannual scale ( $\geq 2$  years). The largest skill is observed for the “wet” states 4–6 and state 1. Surprisingly, ISI could provide a significant information at interannual time scale for state 2 and 6. In fact, the standard deviation of ISI is annually modulated (Fig. 9 SI), with largest values between mid-December and late March, that is around the peak of the austral summer monsoon but also at interannual time scale (not shown). The standard deviation of ISI in DJF is significantly correlated with DJF Niño 4 ( $r = -0.39$ , significant at the one-sided 95 % significance level according to a random-phase test). We can imagine that a strong intraseasonal variability,

partly related to cold ENSO events, could promote for example more state 6 by setting the conditions for SW shift of the SPCZ. A intraseasonal time scale (Fig. 13c), the skill is usually similar for AN + ISI and AN + ISI + Niño 4.

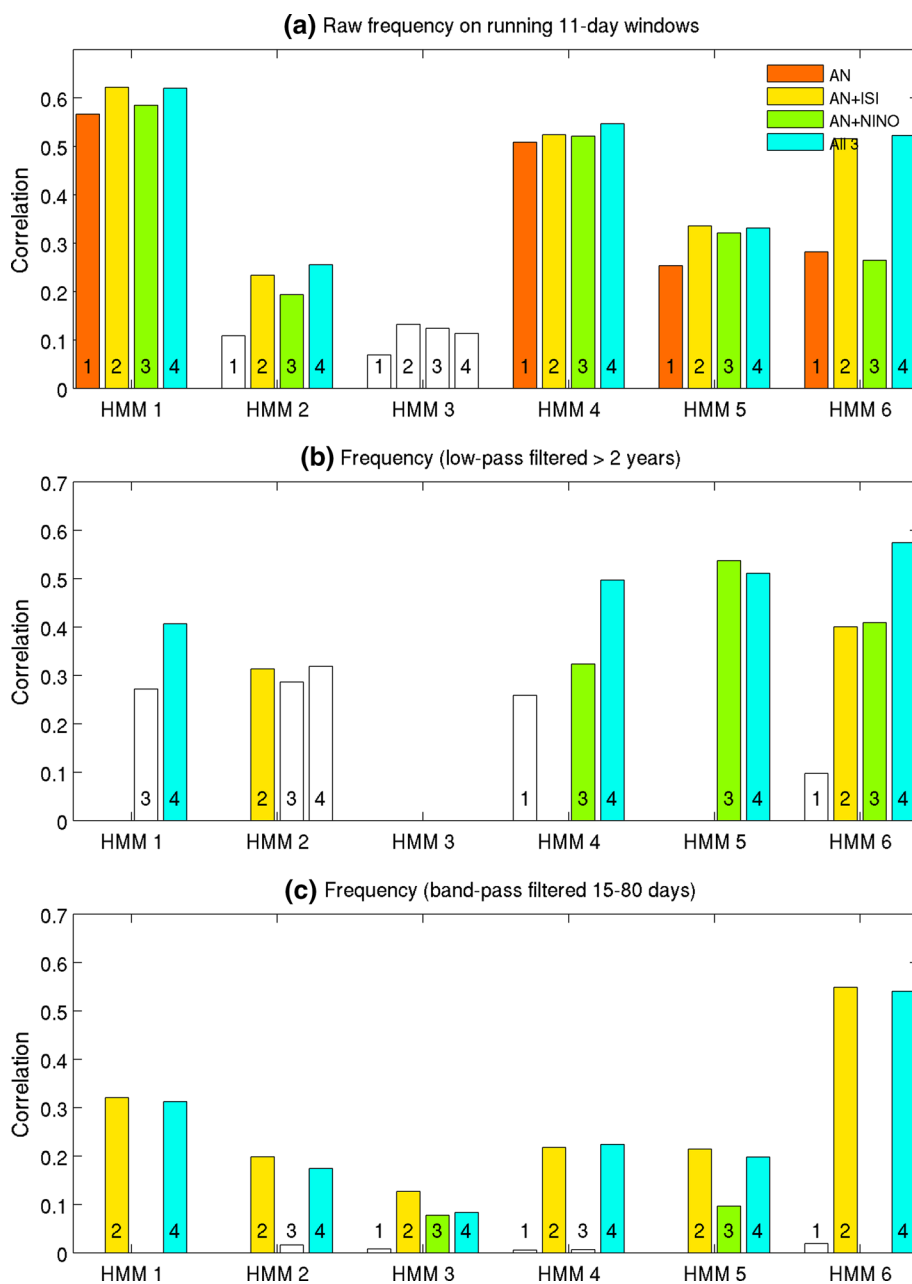
Figure 14 shows the modulation of cross-validated skill for 2 NHMM models—AN + Niño 4 and the full model including the three different predictors—on running 91-days window. The skill peaks clearly around the austral spring, near the transition between dry and wet season at least for states 5 and 6 while it peaks latter from February to May for state 2. State 1 and 4 has a weaker skill while state 3 is never accurately specified. The inclusion of the three predictors, adding intraseasonal variability, has a clear positive impact, especially for state 4 and 6 in September–December, and for state 2 from February to May (Fig. 14b). The benefit is less obvious for states 2,5 and state 3 remains impossible to specify using the three indices. This failure could be attributed to the tremendous impact of synoptic waves for this specific state and its poor modulation, if any, by Niño 4 and ISI.

### 5.2 Daily rainfall

The two models including AN + NINO and AN + NINO + ISI are further investigated to analyse the potential predictability of rainfall. We computed also cross-validated hindcasts for two lead times by using NINO and ISI 30 and 60 days before daily rainfall (not shown). We computed also the skill for two different running averages—31 and 91 days—and for the amount (and also frequency of wet days which gives similar behavior, not shown). Figure 15 shows the skill of standardized anomaly index, i.e. the spatial average of interannual variability of 55 rain gauges, for running 31- and 91-day windows. The skill of the full model is clearly the best for 31-day sampling (Fig. 15a). This advantage is still visible for 91-day windows (Fig. 15b) suggesting that there is perhaps not a perfect linear cancellation associated with alternating anomalies of ISI. The skill is at maximum between September and late May with highest values around October. With a 31-day sampling, the separate maxima are probably related to random uncertainty. The benefit of the inclusion of ISI almost vanishes for lead time of 30 and 60 days (not shown).

One of the advantage of the HMM approach is to provide daily sequences of rainfall, thus offering the possibility of analyse how the predictable signal is conveyed toward finer scales than seasonal amounts. Figure 16 explores the skill of 2 intraseasonal quantities: the frequency of wet days receiving at least the amount corresponding to the local 90 % percentile of wet days and the frequency of dry days in dry spells lasting at least 5 days. The skill for frequency of extreme wet days and the long

**Fig. 13** Cross-validated skill of states' frequency given three different predictors; the replication of the mean annual cycle of rainfall spatially averaged across the 55 stations low-pass filtered over 90 days (=AN), Niño 4 times series (=NINO), and the intraseasonal OLR index (=ISI) combined into four different models (Model 1 = AN; Model 2 = AN + ISI; Model 3 = AN + NINO; Model 4 = AN + NINO + ISI. **a** Daily frequency are smoothed by a running 11-day window, **b** smoothed time series of **a** is low-pass filtered  $\geq 2$  years, **c** smoothed time series of **a** is band-pass filtered between 15 and 80 days. The states are defined using an NHMM with the predictors with zero lead with training over 25 years and verification on the remaining 5 years, which serve to get the hindcast states. One hundred simulations are done for each set of predictors. The *colored bars* are significant positive correlations at the one-sided 95 % level according to a random-phase test and negative correlations are not displayed



dry spells matches rather well with the one obtained with amounts of rainfall (Fig. 15b), illustrating the ability of NHMM to reveal possible modulations on the translation of predictable signals from the comprehensive amounts toward intraseasonal characteristics.

## 6 Conclusion and discussion

The HMM yields a state-based description of daily rainfall recorded on a network of 55 stations across NC which help interpret local to regional-scale variability of atmospheric circulation at a tropical location not directly impacted by

the monsoons. NC is an example of a tropical island largely dominated by easterly trade winds.

The three most persistent of the 6 states (states 1, 2 and 4; Table 1) are associated with an atmospheric trade regime (Fig. 7). They account for 75 % of the total number of days. The general dryness of state 1 (Figs. 4a, 5a) is associated with regional-scale subsidence under the eastern edge of a subtropical anticyclone centered over Australia in the mean (Fig. 7a). The weak trades coupled with the subsidence prevent the occurrence of windward-side rainfall related to wind-terrain interaction. This state is the most prevalent from mid-May to mid-December and its frequency of occurrence exceeds 50 % from August to

**Fig. 14** Cross-validated skill of states' frequency on running 91-day windows given three different predictors; the replication of the mean annual cycle of rainfall spatially averaged across the 55 stations low-pass filtered over 90 days (=AN), Niño 4 times series (=NINO), and the intraseasonal OLR index (=ISI) combined into two different models; **a** AN + NINO and **b** AN + NINO + ISI. The states are defined using an NHMM with the predictors with zero lead with training over 25 years and verification on the remaining 5 years, which serve to get the hindcast states. One hundred simulations are done for each set of predictors. The *dots* indicate positive correlation at the one-sided 95 % level according to a random-phase test (Janicot et al. 1996). The *labels on abscissa* refer to the first day of each month

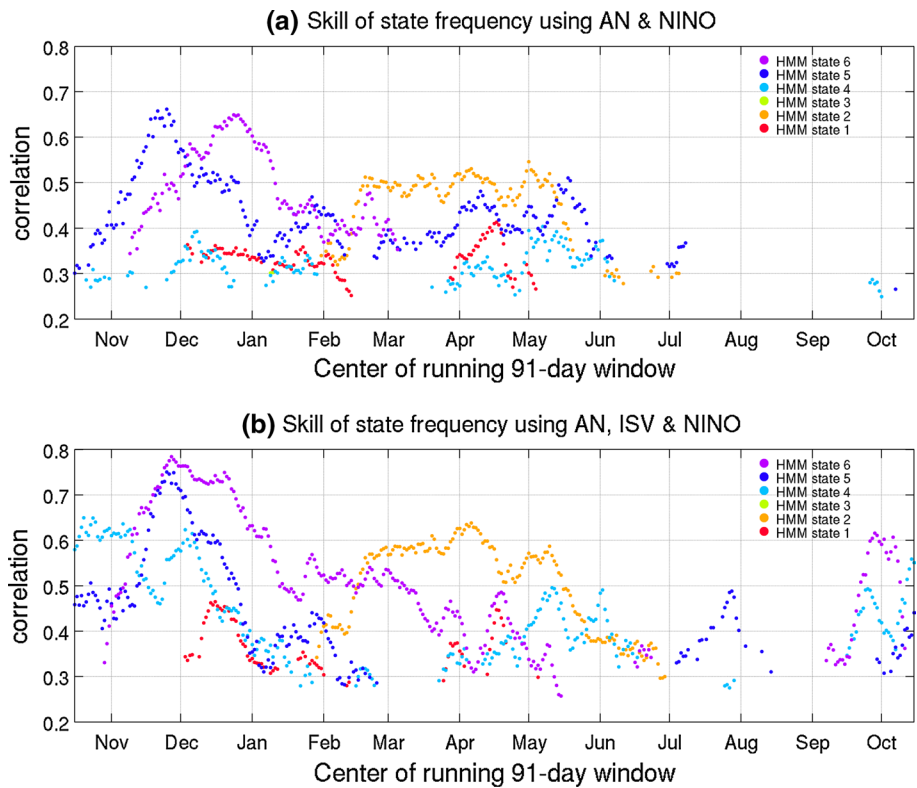
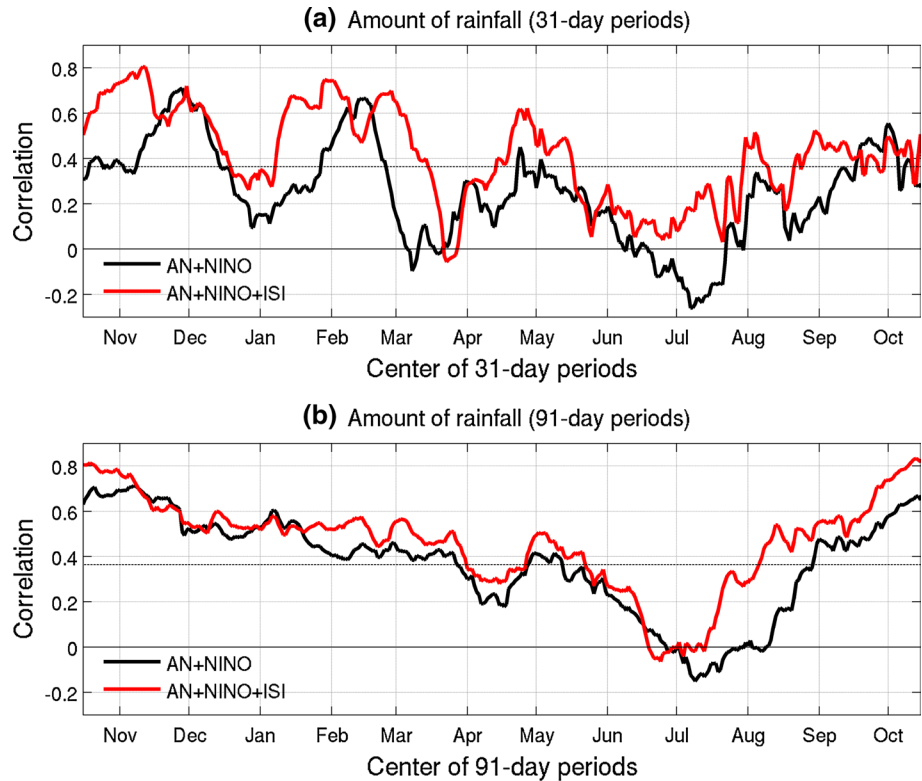


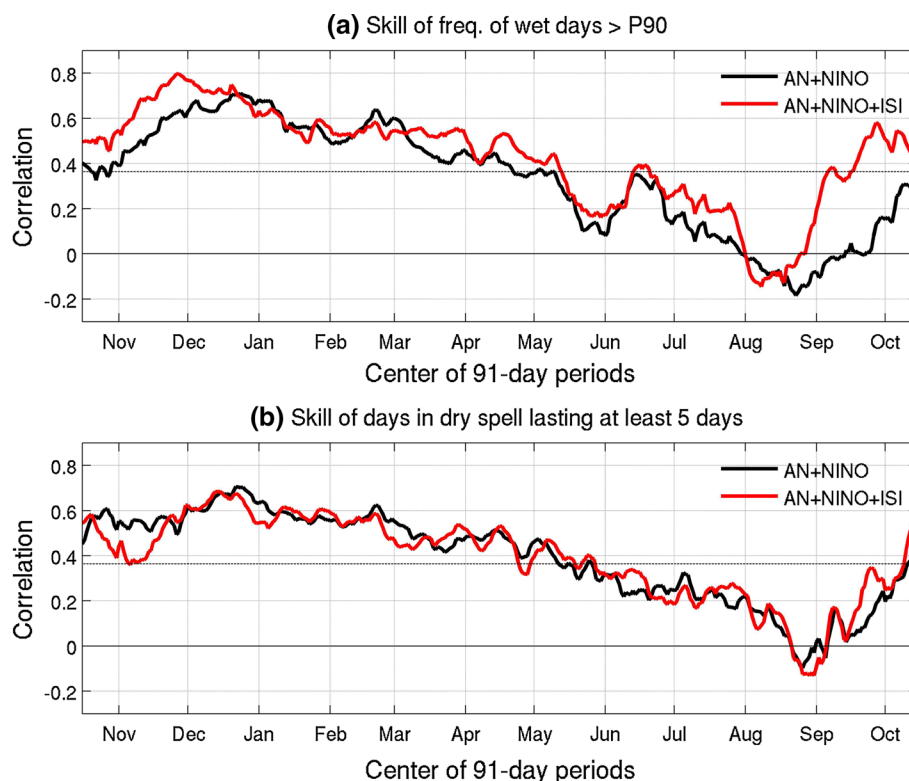
**Fig. 15** Correlation between observed standardized anomaly index (=spatial average of the standardized anomalies of amount of rainfall of the 55 stations) of **a** running 31-day and **b** 91-day windows and hindcast from two NHMM models. The states are defined using an NHMM with the predictors with training over 25 years and verification on the remaining 5 years, which serve to get the hindcast states. One hundred simulations are done for each set of predictors. The *dashed horizontal line* represents the one-sided 95 % significance level with 29 degrees of freedom. The *labels on abscissa* refer to the first day of each month



October (Fig. 6). The subtropical anticyclone shifts close to New Zealand in state 2 and 4 (Fig. 7b, d) and ESE (state 2) and ENE (state 4) trades blow stronger than in state 1

(Fig. 8a, b, d); this shift is related primarily to the annual cycle since both states 2 and 4 peak around austral summer (Fig. 6). Stronger ENE trades in state 4, i.e. aligned more

**Fig. 16** Correlation between observed standardized anomaly index (=spatial average of the standardized anomalies of amount of rainfall of the 55 stations) of running 91-day: **a** frequency of wet days  $\geq 90\%$  percentile and **b** dry days included in dry spells lasting at least five consecutive days from two NHMM models. The states are defined using an NHMM with the predictors with training over 25 years and verification on the remaining 5 years, which serve to get the hindcast states. One hundred simulations are done for each set of predictors. The *dashed horizontal line* represents the one-sided 95 % significance level with 29 degrees of freedom. The *labels on abscissa* refer to the first day of each month



perpendicular to the island, accentuate the windward/leeward dipole across the central range, i.e. leading to light (in state 2) and moderate (in state 4) rainfall mostly along the eastern coast (Figs. 4b, d, 5b, d). The atmospheric regimes associated with the rainfall states 1, 2 and 4 are relatively stable across the annual cycle (Figs. 2–7, SI). This is not trivial since the HMM states are derived purely from station rainfall across NC; they represent spatially correlated rainfall patterns driven by regional- to large-scale circulations, though the latter are not necessarily unique. States 1, 2 and 4 seem to be associated with roughly the same atmospheric regime, i.e. anticyclonic subsidence coupled with more or less intense trades blowing mostly from SE to ESE (states 1 and 2) and ENE (states 4) throughout the calendar year.

The cyclonic states (state 3, 5 and 6), are related to different atmospheric regimes according to the season (Fig. 7c, e, f). Most of the rainfall in state 3 is light and restricted to the SW part of ‘Grande Terre’, associated with the northernmost edge of extratropical cold fronts during winter (Figs. 4c, 5c). States 5 and 6 are infrequent (<15 % of days) but contribute almost 70 % of total rainfall (and up to 85 % on the northern part of the leeward coast, not shown). Both are related to a low level cyclonic eddy or NW–SE trough located west of or over NC (Fig. 8e, f) implying a large influx of moist and unstable air from equatorial latitudes and the states 5 and especially 6 include the most powerful TCs. State 5 is wetter in the south of NC

(Figs. 4e, 5e) while state 6 is very wet everywhere (Figs. 4f, 5f). Two different atmospheric regimes can be distinguished: the first, exemplified by state 3, is associated with transient extratropical winter storms passing to the south of NC; the second one, during summer, is exemplified by state 6, and is similar to “shifted SPCZ” mode identified by Matthews (2012), Van Der Wiel et al. (2015) and the “tropical” regime identified by Lefèvre et al. (2010). This mode involves a southwestward shift of the SPCZ on various time scales (Matthews 2012), and NC receives a large influx of equatorial air when the cyclonic vorticity anomaly is located between Australia and NC.

The HMM state frequencies are modulated on various time scales. As already noted, the annual cycle strongly modulates the state frequencies with an out-of-phase relationship between state 1 on one hand and state 2, 4–6 on the other (Fig. 6). State 3 is unique in peaking in austral winter. Overall, the mean annual cycle of the other states reveal a weak asymmetry between the maximum (minimum) frequency of state 5–6 (state 1) around late February and its minimum (maximum) around mid-September. The asymmetric annual cycle may be related to the slow southward and eastward progression of deep convection from India in July to the SPCZ region in January (Meehl 1987; Vincent 1994). The occurrence of states 1, 3, 5 and 6 is clearly modulated at synoptic scale by eastward propagating Rossby waves travelling along the Australian subtropical Jet Stream (Fig. 10), which acts as a waveguide

(Ambrizzi et al. 1995). In austral summer, eastward propagating Rossby waves may cause a “shifted” (in states 5 and 6) or “intense” (in state 3) SPCZ as argued by Matthews (2012), Van Der Wiel et al. (2015), with an influx of moist and unstable equatorial air toward NC (stronger in state 6 than in state 5). In austral winter, Rossby waves can give rise to transient enhancement of the subsidence on the eastern edge of an anticyclone centered over Australia (in state 1), or to transient synoptic perturbations travelling on a storm track near 30°S and inducing southerlies toward NC, and light rainfall south of “Grande Terre” (in state 3). On the intraseasonal time scale, the MJO influences the equatorial western Pacific (Wheeler and Hendon 2004) and the climatological axis of the SPCZ, located 10°–15° northeast of NC (Matthews and Li 2005). However, the MJO’s direct impact on the state occurrence frequencies is found to be weak, presumably due to southward geographical location of NC. Nevertheless, the occurrence of state 6 is found to be strongly modulated by local-scale intraseasonal variability (Fig. 12), although this is not directly tied to the MJO. This aspect deserves further investigation.

On the interannual time scale, a primary driver of state frequency is ENSO events with an enhanced sensitivity to central Pacific events (Barbero and Moron 2011) in austral spring; at this time the seasonal warming of SST near the dateline combines with the seasonal growth of ENSO events to induce anomalous subsidence over NC during warm events. The impact of central ENSO events is seen in the running correlations of state frequency with Niño 4 (Fig. 12) and the anomaly composites (Fig. 9). Figure 11 shows that warm ENSO events promote more (less) states 1–2 (states 4–6) from austral spring to autumn, while cold ENSO events lead to the reverse. The out-of-phase ENSO relationship between the contrasting states 1 and 6 is strongest toward the end of calendar year. Thus, the impact of ENSO events on NC rainfall is clearest during this season because the driest (state 1) and wettest (state 6) states are inversely correlated to Niño 4 (Fig. 11). The composites of OLR and moisture fluxes anomalies for state 2 (Fig. 9b) and 6 (Fig. 9f) is approximately out-of-phase and exhibits the largest coverage of statistically significant anomalies. Their spatial structure resembles the Rossby wave response to an ENSO anomaly in equatorial diabatic heating (Gill 1980). During warm ENSO events, there is an eastward shift of the ascending branch of Walker cell with an anomalous subsidence to the west and southwest of the equatorial surface warming (Karoly 1989; Kidson and Renwick 2002; Lau and Nath 2000; Trenberth 1976; Van Loon 1984). The stationary response associated with ENSO is especially clear for state 2, with a tripolar OLR anomaly pattern across the climatological location of the SPCZ (Fig. 9b), consistent with the mean atmospheric response during warm ENSO events. In contrast, while

state 6 (Fig. 9f) is consistent with the stationary response during cold ENSO events, it is seen to be mixed with strong transient eastward-propagating Rossby waves (Fig. 10f). The mix of transient and stationary responses to ENSO events is also seen in state 1, which is more frequent during El Niño events (Fig. 11) and which exhibits a strong eastward propagating wave component. Overall, the HMM approach reveals, without any a priori temporal filtering, that central ENSO impact may work through either stationary and transient atmospheric motions in the subtropical SW Pacific. The interplay between both responses warrants clearly more analyses.

The seasonally dependent ENSO teleconnections imply potential predictability of state occurrence and the associated rainfall. We constructed NHMMs with various predictors based on the Niño 4 SST index, together with an intraseasonal OLR index. At zero lead, intraseasonal variability clearly increases the skill of the NHMM in predicting state frequency and rainfall, especially for state 6 before the end of the calendar year (Figs. 13, 14). Intraseasonal modulations also increase the skill of running 91-day amounts (Fig. 15), though weakly, which could only arise if the impact of intra-seasonal variability on NC rainfall is non-linear (that is inhibiting the full cancellation of positive and negative impact in a time frame including one entire intra-seasonal oscillation). The practical use of this information in sub-seasonal to seasonal forecasts will be contingent on the ability to forecast the local intra-seasonal index which is unrelated to large-scale MJO index and is beyond the scope of this study. However, Niño 4 already provides some skill for applications as intensity of fire season in austral Spring predicted from austral Winter season (Moron et al. 2013).

**Acknowledgments** The early stages of this research (V.M., R.B.) were funded by a french ANR BIODIV grant (INCendies en Nouvelle Caldonie). A.W.R. was supported by MURI Grant N00014-12-1-0911 from the US Office of Naval Research.

## References

- Ambrizzi T, Hoskins BJ, Hsu H-H (1995) Rossby wave propagation and teleconnection patterns in the austral winter. *J Atmos Sci* 52:3661–3672
- Barbero R, Moron V (2011) Seasonal to decadal modulation of the impact of El Niño/Southern Oscillation on New Caledonia (SW Pacific) rainfall. *J Geophys Res* 116:D23111
- Barbero R, Moron V, Mangeas M et al (2011) Relationships between MODIS and ATSR fires and atmospheric variability in New Caledonia (SW Pacific). *J Geophys Res* 116:D21110
- Basher RE, Zheng X (1995) Tropical cyclones in the south west Pacific: spatial patterns and relationships to Southern Oscillation and sea surface temperature. *J Clim* 8:1249–1260
- Chang CP, Wang Z, McBride J, Liu CH (2005) Annual cycle of Southeast Asia—maritime continent rainfall and the asymmetric monsoon transition. *J Clim* 18:287–301

- Delcroix T, Lenormand O (1997) ENSO signals in the vicinity of New Caledonia, South Western Pacific. *Oceanol Acta* 20:481–491
- Fischer M, Dewitte B, Maitrepierre L (2004) A non-linear statistical downscaling model: El Niño/Southern Oscillation impact on precipitation over New Caledonia. *Geophys Res Lett* 31:L16204
- Folland CK, Renwick JA, Salinger MJ, Mullan AB (2002) Relative influences of the interdecadal Pacific oscillation and ENSO on the South Pacific Convergence Zone. *Geophys Res Lett* 29:1643
- Gill AE (1980) Some simple solutions for heat-induced tropical circulation. *Q J Meteorol Soc* 106:447–462
- Haffke C, Magnusdottir G (2013) The South Pacific Convergence Zone in three decades of satellite images? *J Geophys Res (Atmos)* 118:10839–10849
- Janicot S, Moron V, Fontaine B (1996) Sahel droughts and ENSO. *Geophys Res Lett* 23:515–518
- Jourdain NC, Sen Gupta A, Taschetto AS, Ummerhofer CC, Moise AF, Ashok K (2013) The Indo-Australia monsoon and its relationship to ENSO and IOD in reanalysis data and the CMIP3/CMIP5 simulations. *Clim Dyn* 41:30733102. doi:10.1007/s00382-013-1676-1
- Kanamitsu M, Ebisuzaki W, Woolen J et al (2002) NCEP-DOE AMIP-II reanalysis (R-2). *Bull Am Meteorol Soc* 83:1631–1643
- Karoly J (1989) Southern hemisphere circulation features associated with El Niño-Southern Oscillation events. *J Clim* 2:1239–1252
- Kidson JW, Renwick JA (2002) The southern hemisphere evolution of ENSO during 1981–99. *J Clim* 15:847–863
- Lau NC, Nath MJ (2000) Impact of ENSO on the variability of the Asian–Australian monsoons as simulated in GCM experiments. *J Clim* 13:4287–4309
- Lefèvre J, Marchesiello P, Jourdain NC, Menkes C, Leroy A (2010) Weather regimes and orographic circulation around New Caledonia. *Mar Pollut Bull* 61:413–431
- Leroy A (2006) Utilisation des prévisions saisonnières en Nouvelle-Calédonie. Note de la DP no. 6, Direction de la Météorologie, MétéoFrance, 169 pp
- Leroy A, Céron JP (2007) Un défi de la prévision saisonnière: la descente d'échelle. *La Nouvelle-Calédonie, un exemple à suivre. La Météorol* 58:36–44
- Leroy A, Wheeler MC (2008) Statistical prediction of weekly tropical cyclone activity in the southern hemisphere. *Mon Weather Rev* 136:3637–3654
- Liebmann B, Smith CA (1996) Description of a complete (interpolated) outgoing longwave radiation dataset. *Bull Am Meteorol Soc* 77:1275–1277
- Madden RA, Julian PR (1971) Description of a 40–50 day oscillation in the zonal wind in the tropical Pacific. *J Atmos Sci* 28:702–708
- Madden RA, Julian PR (1994) Observations of the 40–50 day tropical oscillation—A review. *Mon Weather Rev* 122:814–837
- Mathews AJ (2012) A multiscale framework for the origin and variability of the South Pacific Convergence Zone. *Q J Meteorol Soc* 138:1165–1178
- Mathews AJ, Li HYY (2005) Modulation of station rainfall over the Western Pacific by the Madden–Julian oscillation. *Geophys Res Lett* 32:L14827
- Meehl GA (1987) The annual cycle and interannual variability in the tropical Pacific and Indian Ocean regions. *Mon Weather Rev* 115:27–50
- Morlière A, Rébert JP (1986) Rainfall shortage and El Niño-Southern Oscillation in New Caledonia, southwestern Pacific. *Mon Weather Rev* 114:1131–1137
- Moron V, Vautard R, Ghil M (1998) Trends, interdecadal and interannual oscillations in global sea surface temperatures. *Clim Dyn* 14:545–569
- Moron V, Barbero R, Mangeas M et al (2013) Prediction of September–December fire in New Caledonia (SouthWestern Pacific) using July Niño-4 sea surface temperature. *J Appl Meteorol Clim* 52:623–633
- Nicot JB, Delcroix T (2000) ENSO-related precipitation changes in New Caledonia, southern Pacific: 1969–98. *Mon Weather Rev* 128:3001–3006
- Revell CG, Goulter SW (1986) South Pacific tropical cyclones and the Southern Oscillation. *Mon Weather Rev* 114:1138–1145
- Reynolds RW, Rayner NA, Smith TM et al (2002) An improved in situ and satellite SST analysis for climate. *J Clim* 15:1609–1625
- Robertson AW, Kirshner S, Smyth P (2004) Downscaling of daily rainfall occurrence over Northeast Brazil using a Hidden Markov Model. *J Clim* 17:4407–4424
- Robertson AW, Kirshner S, Smyth P et al (2006) Subseasonal-to-interdecadal variability of the Australian monsoon over North Queensland. *Q J Meteorol Soc* 132:519–542
- Robertson AW, Moron V, Swarimoto Y (2009) Seasonal predictability of daily rainfall statistics over Indramayu district, Indonesia. *Int J Climatol* 29:1449–1462
- Robertson AW, Moron V, Qian JH et al (2011) The maritime continent monsoon. In: Chang CP et al (eds) *The global monsoon system: research and forecast*, 2nd edn, World Scientific Publishing Co., New Jersey, pp 85–98
- Sinclair MR (1993) Synoptic-scale diagnosis of the extratropical transition of a SouthWest Pacific tropical cyclone. *Mon Weather Rev* 121:941–960
- Trenberth KE (1976) Spatial and temporal variations in the Southern Oscillation. *Q J R Meteorol Soc* 102:639–653
- Trenberth KE (1991) Storm tracks in the Southern Hemisphere. *J Atmos Sci* 48:2159–2178
- Van Der Wiel K, Mathews AJ, Stevens DP, Joshi MM (2015) A dynamical framework for the origin of the diagonal South Pacific and South Atlantic Convergence Zones. *Q J R Meteorol Sci*. doi:10.1002/qj.2508
- Van Loon H (1984) The Southern Oscillation. Part III: associations with the trades and with the trough in the westerlies of the South Pacific ocean. *Mon Weather Rev* 112:947–952
- Vera C (2003) Interannual and interdecadal variability of atmospheric synoptic-scale activity in the Southern Hemisphere. *J Geophys Res* 108:8077
- Vincent DG (1994) The South Pacific Convergence Zone (SPCZ): a review. *Mon Weather Rev* 122:1949–1970
- Vincent EM, Lengaigne M, Menkes CE, Jourdain NC, Marchesiello P, Madec G (2011) Interannual variability of the South Pacific Convergence Zone and implications for tropical cyclone genesis. *Clim Dyn* 36:1881–1896
- Wheeler MC, Hendon HH (2004) An all-season real-time multivariate MJO index: development of an index for monitoring and precipitation. *Mon Weather Rev* 132:1917–1932
- Wheeler MC, McBride J (2005) Australian–Indonesian monsoon. In: Lau WKM, Waliser DE (eds) *Intraseasonal variability in the atmosphere–ocean climate system*. World Scientific Press, New Jersey, pp 125–173
- Widlansky MJ, Webster PJ, Hoyos CD (2011) On the location and orientation of the South Pacific Convergence zone. *Clim Dyn* 36:561–578
- Wilks DS, Wilby RL (1999) The weather generation game: a review of stochastic weather models. *Prog Phys Geogr* 23:329–357